



STUDY OF ALL-FIBER SENSORS FOR SALINITY AND TEMPERATURE SIMULTANEOUS MEASUREMENT

Tanushree Selokar

Tese apresentada ao Programa de Pós-Graduação em Instrumentação e Óptica Aplicada, do Centro Federal de Educação Tecnológica Celso Suckow da Fonseca, CEFET/RJ, e Universidade Federal Fluminense, UFF, como parte dos requisitos necessários à obtenção do título de Doutor em Instrumentação e Óptica Aplicada.

Orientador: Maria Thereza Miranda Rocco Giraldi

Rio de Janeiro
Novembro 2021

STUDY OF ALL-FIBER SENSORS FOR SALINITY AND TEMPERATURE SIMULTANEOUS MEASUREMENT

Tese apresentada ao Programa de Pós-Graduação em Instrumentação e Óptica Aplicada, do Centro Federal de Educação Tecnológica Celso Suckow da Fonseca, CEFET/RJ, e Universidade Federal Fluminense, UFF, como parte dos requisitos necessários à obtenção do título de Doutor em Instrumentação e Óptica Aplicada.

Tanushree Selokar

Banca Examinadora:

Presidente, Professora Dra. Maria Thereza Miranda Rocco Giraldi (IME)
(Orientador)

Professor Dr. Hypolito José Kalinowski (UFF)

Professora Dra. Maria Aparecida Gonçalves Martinez (CEFET/RJ)

Professor Dr. João Crisóstomo Weyl Albuquerque Costa (UFPA)

Professora Dra. Cindy Stella Fernandes (UNIFESSPA)

Rio de Janeiro
Novembro 2021

Ficha catalográfica elaborada pela Biblioteca Central do CEFET/RJ

S468 Selokar, Tanushree
Study of all-fiber sensors for salinity and temperature simultaneous measurement / Tanushree Selokar. — 2021.
97f. + apêndice : il. color. , enc.

Tese (Doutorado) Centro Federal de Educação Tecnológica Celso Suckow da Fonseca , 2021.
Bibliografia : f. 91-97
Orientadora: Maria Thereza Miranda Rocco Giraldi

1. Fibra óptica. 2. Sensoriamento remoto. 3. Controle de temperatura. 4. Salinidade – Controle. I. Giraldi, Maria Thereza Miranda Rocco. (Orient.). II. Título.

CDD 621.3692

Elaborada pela bibliotecária Tania Mello – CRB/7 nº 5507/04

DEDICATION

To my Daughter and my Family.

Acknowledgement

I would like to special thanks to my supervisor, Prof. Dr. Maria Thereza for her support, valuable guidance and patience over the past four years. She is always ready to help me, whenever I have problems about my project work and accompany with me during experimental studies at IME lab. I am so impressed by Prof. Thereza for her depth and profound theoretical knowledge on optical fibers and she used to share her ideas and suggestion, which greatly help me develop a thorough understanding of the subject. Along the research work, professor listens my personal issue and provide all the support which she can provide.

I would also like to thank Prof. Dr. Marcos Franco for the kindness to allow me to use the simulation software. His group members are very kind and provide the necessary information about the simulation software, thanks to all team members.

A very special thanks to Prof. Dr. Maria Aparecida Martinez for her great support in my research work in her Photonics lab at CEFET/RJ.

I appreciate Dr. Jesse Werner Costa for his support in laboratory and my simulation work.

My thanks go to all teachers who taught me during my first year PhD course work and their practical and in-depth subjects knowledge helps me for research work.

Thank you to all my dear friends who helps me in lab and office, as I was struggling with the new language.

I was never in trouble for registration process, renew of RNE card and other related work; it's because of Fernando. I thanks to Fernando who helps and extends all support and provide all the necessary documents for my visa and registration purposes and specially translate my mail from Portuguese to English language.

Thanks to Alberto R. da Cruz for his friendship and support in IME lab. I really enjoy working with him. I have had a very happy life with my Indian colleagues and my lab mate during my PhD study.

Special Thanks to my husband and daughter Ovi for always being with me and supporting me in past four years.

I would like to express my gratitude to my parents for all the support for all these years!

ABSTRACT

STUDY OF ALL-FIBER SENSORS FOR SALINITY AND TEMPERATURE SIMULTANEOUS MEASUREMENT

In this work the basic device is a core diameter mismatch (CDM) structure composed of small simple arrangements of singlemode (SMF) and multimode fibers and the balloon structure made of bent singlemode fiber. The proposed sensors are easy to fabricate, simple, cost effective and are safe for the environment.

In this work, the simple all-fiber sensors are developed to measure salinity and temperature using multimodal interference, with applications as temperature and salinity sensor. We demonstrate four types of CDM structures with balloon shaped SMF sensor for individual and simultaneous measurement of salinity and temperature. By measuring the wavelength shifts spectra in each scheme, simultaneous measurement of temperature and salinity could be achieved. Simulations for the CDM structures were performed by using the Beam Propagation software.

Among all the CDM structures, the SM1SM2S sensor shows the best salinity sensitivity with 402 pm/%NaCl. For the temperature measurements, the SM1SM1S sensor shows the best sensitivity among all the structures with a maximum value of 377.62 pm/°C. With the combination of the CDM and balloon shaped sensor for salinity measurements, the SM1SM1S and balloon shaped sensor depicts the best sensitivity among all the other structures with a value of 168 pm/% NaCl. For the temperature measurements, the SM1M2S structure combined to the balloon structure shows a great sensitivity with a maximum value of 735.6 pm/°C. Concerning the simultaneous measurement, the SM1SM2S with the balloon shaped sensor presents a maximum sensitivity of 2.86 dB/°C at 10% NaCl saline solution.

Keywords: Core Diameter Mismatch, balloon structure, Multimode Interference, salinity and temperature sensor.

RESUMO

STUDY OF ALL-FIBER SENSORS FOR SALINITY AND TEMPERATURE SIMULTANEOUS MEASUREMENT

Neste trabalho, o dispositivo básico é uma estrutura de descasamento de diâmetro de núcleo (CDM) composta por pequenos arranjos simples de fibras monomodo e fibras multimodo e a estrutura em balão, que é feita de fibra monomodo curvada. Os sensores propostos são fáceis de fabricar, simples, econômicos e seguros para o meio ambiente.

Neste trabalho, sensores simples totalmente a fibra são desenvolvidos para medir salinidade e temperatura usando interferência multimodal, com aplicações como sensor de temperatura e de salinidade. Demonstramos quatro tipos de estruturas de CDM com o sensor em forma de balão para medição individual e simultânea de salinidade e temperatura. Medindo-se os espectros com a variação do comprimento de onda de cada sensor, pode-se obter a medição simultânea de temperatura e salinidade. Simulações das estruturas com CDM foram realizadas usando-se o software de propagação do feixe (BeamProp).

Entre todas as estruturas CDM, o sensor SM1SM2S de salinidade mostrou a melhor sensibilidade com um valor de 402 pm/%NaCl. Para as medições de temperatura, o sensor SM1SM1S apresentou a melhor sensibilidade entre todas as estruturas com um valor máximo de 377,62 pm/°C. Com a combinação da estrutura CDM e o balão para medições de salinidade, o sensor SM1SM1S com o balão mostrou a melhor sensibilidade entre todas as outras estruturas com um valor de 168pm/%NaCl. Para as medições de temperatura, a estrutura SM1M2S combinada à estrutura do balão apresentou uma grande sensibilidade com valor máximo de 735,6 pm/°C. Para a medição simultânea, o sensor com a estrutura SM1SM2S e o balão mostrou uma sensibilidade máxima de 2.86 dB/°C em 10% de NaCl.

Palavras-chave: Descasamento de diâmetro de núcleo, estrutura em balão, Interferência Multimodal, sensor de salinidade e de temperatura.

List of Figures

Figure 1:	Typical optical fiber cable……	20
Figure 2:	Basic components of an optical fiber sensor……	21
Figure 3:	An extrinsic optical fiber sensor……	23
Figure 4:	An intrinsic optical fiber sensor……	23
Figure 5:	Fiber optic technician testing the system response with a flask of liquid nitrogen for pipeline leakage……	25
Figure 6:	Optical sensor attached on the wind turbine blades……	26
Figure 7:	Endoscopic instrument with an optical fiber sensor……	26
Figure 8:	SMS structure, propagation profile diagram, transmission along the axis……..	31
Figure 9:	(a) Field profile within the multimode waveguide showing (b) self-imaging of the input field……..	33
Figure 10:	Singlemode –multimode –singlemode (SMS) structure……	37
Figure 11:	(a) Beam propagation model of SMS structure, (b) propagation field and (c) transmission along the axis……	38
Figure 12:	Singlemode–multimode–singlemode–multimode–singlemode (SMSMS) structure…….	39
Figure 13:	(a) Model structure of SMSMS, (b) propagation of light and (c) transmission along the axis…….	40
Figure 14:	Singlemode–multimode1–singlemode–multimode2–singlemode (SM1SM2S) structure…….	41
Figure 15:	(a) Beam Propagation software model of SM1SM2S structure, (b) propagation, (c) transmission along the axis……	42

Figure 16: Singlemode–Multimode1–Multimode2–Singlemode (SM1M2S) structure…… 43

Figure 17: (a) Model structure of SM1M2S in Beam propagation software, (b) light propagation and (c) transmission along the axis……. 43

Figure 18: Schematic diagram of the balloon shaped sensor…… 44

Figure 19: Transmission spectrum of the balloon shaped structure for different diameters values…… 45

Figure 20: Flow chart of working of Beam Propagation software…… 49

Figure 21: Outlook of Beam Prop Software……. 50

Figure 22: Global setting window……. 50

Figure 23: Simulation Parameter window…… 51

Figure 24: a) Cleaving process, (b) Fusion process, (c) Fibers fusion spliced… 52

Figure 25: Photo of the Balloon sensor used for performing the experiments… 54

Figure 26: Schematic diagram of the experimental setup with the combination of CDM and Balloon shaped sensor…… 56

Figure 27: Experimental setup of CDM structure for measurement of salinity, temperature and simultaneous measurement……. 56

Figure 28: Experimental setup of Balloon and CDM sensor for measurement of salinity, temperature and simultaneous measurement……. 57

Figure 29: (a) Transmitted spectrum for the change in salinity percentage for the SM1S sensor, (b) wavelength variation with salinity at Dip 1…… 58

Figure 30: (a) Transmitted spectrum for the change in salinity percentage for the SM2S sensor, (b) wavelength variation with salinity at Dip 1…… 59

Figure 31: (a) Transmitted spectrum for the change in salinity percentage for the SM1SM1S sensor, (b) wavelength variation with salinity at Dip 3… 60

Figure 32: (a) Transmitted spectrum for the change in salinity percentage for the SM1SM2S sensor, (b) wavelength variation with salinity at Dip 5… 61

Figure 33: (a) Transmitted spectrum for the change in salinity percentage for the SM1M2S sensor, (b) wavelength variation with salinity at Dip 3… 61

Figure 34: (a) Transmitted spectrum for the change in salinity percentage for the combination of the SM1SM1S and balloon shaped sensor, (b) wavelength variation with salinity at Peak 2…….. 63

Figure 35: (a) Transmitted spectrum for the change in salinity percentage for the combination of the SM1SM2S and balloon shaped sensor, (b) wavelength variation with salinity at Peak 2…… 64

Figure 36: (a) Transmitted spectrum of the combined SM1M2S and balloon shaped sensor for salinity, (b) wavelength variation at Peak 1…… 64

Figure 37: (a) Transmitted SM1S Sensor spectrum variation with change in temperature, (b) wavelength as a function of the temperature for Dip 2…… 66

Figure 38: (a) Transmitted SM2S Sensor spectrum variation with change in temperature, (b) wavelength as a function of the temperature for Dip 2…… 67

Figure 39: (a) Transmitted SM1SM1S Sensor spectrum variation with change in temperature, (b) wavelength as a function of the temperature for Dip 1……. 6 68

Figure 40: (a) Transmitted SM1M2S Sensor spectrum variation with change in temperature, (b) wavelength as a function of the temperature for Dip 1…… 69

Figure 41: (a) Transmitted SM1SM2S Sensor spectrum variation with change in temperature, (b) wavelength as a function of the temperature for Dip 69

2……

Figure 42: (a) Transmitted spectrum of the combined SM1SM1S and balloon shaped sensor for temperature variation, (b) loss variation with temperature for Peak 3…… 71

Figure 43: (a) Transmitted spectrum of the combined SM1SM2S and balloon shaped sensor for temperature variation, (b) loss variation with temperature for Peak 1…… 71

Figure 44: (a) Transmitted spectrum of the combined SM1M2S and balloon shaped sensor for temperature variation, (b) wavelength variation with temperature for Dip 1…… 72

Figure 45: (a) Variation in the SM1SM2S and balloon shaped sensor transmitted spectrum for simultaneous measurement at 10% of saline solution, (b) response at Dip 1…….. 75

Figure 46: (a) Variation in the SM1SM2S and balloon shaped sensor transmitted spectrum for simultaneous measurement at 15% of saline solution, (b) response at Dip 1…… 75

Figure 47: (a) Variation in the SM1SM2S and balloon shaped sensor transmitted spectrum for simultaneous measurement at 20% of saline solution, (b) response at Dip 1…….. 76

Figure 48: (a) Variation in the SM1SM2S and balloon shaped sensor transmitted spectrum for simultaneous measurement at 25% of saline solution, (b) response at Dip 1…….. 74

Figure 49: Comparison of experiment and simulation results for the SM1S structure as a salinity sensor…… 78

Figure 50: Comparison of experiment and simulation results for the SM2S structure as a salinity sensor…… 79

Figure 51: Comparison of experiment and simulation results for the SM1SM1S structure as a salinity sensor…… 80

Figure 52: Comparison of experiment and simulation results for the SM1M2S structure as a salinity sensor…… 81

Figure 53: Comparison of experiment and simulation results for the SM1SM2S structure as a salinity sensor…… 82

Figure 54: Comparison of experiment and simulation results for the SM2S structure as a temperature sensor…….. 83

Figure 55: Comparison of experiment and simulation results for the SM1SM1S structure as a temperature sensor…….. 84

Figure 56: Edit symbol Parameter window……. 95

Figure 57: Setting of launch parameter with different launch field…… 95

Figure 58: Pathway monitor window…… 96

Figure 59: Pathway shown in model SMS…… 96

Figure 60: Launch MOST optimizer / scanner window…… 97

List of Tables

Table 1:	Summary of different types of the CDM Structure…….	53
Table 2:	Refractive index with respect to salinity percentage……	55
Table 3:	Characteristics of the sensors for salinity measurement for CDM sensor…….	62
Table 4:	Characteristics of the sensors for salinity measurement for CDM and balloon shaped sensor…….	65
Table 5:	Comparison to some literature sensors for salinity measurement……..	65
Table 6:	Characteristics of the sensors for temperature measurement for CDM sensors only…….	70
Table 7:	Characteristics of the sensors for salinity measurement for CDM and balloon shaped sensor……..	73
Table 8:	Comparison to some previous results published in the literature for temperature measurement…….	73
Table 9:	Characteristics of the SM1SM2S and balloon shaped sensor for simultaneous measurement of temperature and salinity……	77

Acronyms

OFS	Optical Fiber Sensor
FBG	Fiber Bragg Grating
TFBG	Tilted Fiber Bragg Grating
LPG	Long Period Grating
CDM	Core Diameter Mismatch
SMF	Singlemode Fiber
MMF	Multimode Fiber
SMS	Singlemode-Multimode-Singlemode
SMSMS	Singlemode-Multimode-Singlemode-Multimode-Singlemode
SM1M2S	Singlemode-Mutimode1-Multimode2-Singlemode
SM1SM2S	Singlemode-Multimode1-Singlemode-Multimode2-Singlemode
MMI	Multimode Interference
MZI	Mach-Zehnder Interferometer
RI	Refractive Index
L_{eff}	Effective Bending Length
BPM	Beam Propagation Method
BBS	Broad Band Source
OSA	Optical Spectrum Analyzer

SUMMARY

1	**Introduction**	**18**
1.1	Optical fiber sensor	18
1.1.1	Classification of optical fiber sensor…	21
1.2	Motivation	24
1.3	Objectives	28
1.4	Organization of the Thesis	28
2	**Theoretical Analysis**	**30**
2.1	Multimode Interferrence	30
2.2	Reimaging	32
2.2.1	Parabolic Index Fiber	34
2.2.2	Step Index Fiber	35
2.3	Core Diameter Mismatch	36
2.3.1	Singlemode-Multimode-Singlemode structure	36
2.3.2	Singlemode-Multimode-Singlemode-Multimode structure	39
2.3.3	Singlemode-Multimode1-Singlemode-Multimode2 structure	41
2.3.4	Singlemode-Multimode1-Multimode2 structure	42
2.4	Balloon shaped structure	44
2.5	Beam propagation software method	46
3	**Experimental Measurements and Theoretical Modeling**	**52**
3.1	Sensor fabrication process	52
3.1.1	CDM structures	53
3.1.2	Balloon shaped structure	53
3.2	Saline solution preparation	54
3.3	Experimental details	55
3.4	Results for salinity measurement	58
3.4.1	CDM structures only	58
3.4.1.1	SM1S	58
3.4.1.2	SM2S	58

3.4.1.3 SM1SM1S..... 59
3.4.1.4 SM1SM2S..... 60
3.4.1.5 SM1M2S..... 61
3.4.2 CDM structure with the balloon shaped structure..... 62
3.4.2.1 SM1SM1S..... 62
3.4.2.2 SM1SM2S..... 63
3.4.2.3 SM1M2S..... 64
3.5 Results for temperature measurement..... 66
3.5.1 CDM structures only..... 66
3.5.1.1 SM1S..... 66
3.5.1.2 SM2S..... 66
3.5.1.3 SM1SM1S..... 67
3.5.1.4 SM1M2S..... 68
3.5.1.5 SM1SM2S..... 69
3.5.2 CDM structure with the balloon shaped structure..... 70
3.5.2.1 SM1SM1S..... 70
3.5.2.2 SM1SM2S..... 71
3.5.2.3 SM1M2S..... 72
3.6 Results for simultaneous temperature and salinity measurement..... 73
3.7 Simulations result using the BPM software..... 77
3.7.1 Results for salinity simulation..... 78
3.7.1.1 SM1S..... 78
3.7.1.2 SM2S..... 78
3.7.1.3 SM1SM1S..... 79
3.7.1.4 SM1M2S..... 80
3.7.1.5 SM1SM2S..... 81
3.7.2 Results for temperature simulation..... 82
3.7.2.1 SM2S..... 82
3.7.2.2 SM1SM1S..... 83

4 Conclusion and Perspective..... 85
4.1 Suggestions for future work..... 86

4.2 Published and accepted papers..... 87

References..... 88

Appendix..... 95

1 – Introduction

In this chapter, it will be presented a brief history of the optical fiber and optical fiber sensors. After that the classification of optical fiber sensors is presented with their advantages with a short description of the types of sensors. At the end of the chapter, objective and motivation of the research work is also discussed followed by the organization of the thesis.

1.1 – Optical Fiber Sensor

Ever since an ancient time, one of the most important needs of people has been to communicate, which took to the interest in designing and developing communication systems for sending messages from one distant place to another. Optical fibers were available since 1957-1958 and were being used and for making devices that required only a short length of the fiber since then [1]. However, no one was serious about using them for optical communication at that moment. The main problem was that the optical fibers available during the 1960s had such high losses that only 10 % of light entering at one end emerged from the other end of a fiber that was only a few meters long. Since light had to be transported over at least a few kilometers most engineers ignored them for telecommunication applications [2]. It was suggested in 1966 that losses of optical fibers could be reduced drastically by removing impurities from silica glass used to make them, and that such low-losses fibers might be the best choice for optical communication [3]. Indeed, Dr. Charles Kao was awarded one half of the 2009 Physics Noble Prize for his achievements concerning the transmission of light in fibers for optical communication [4].

In 1966, Dr. Kao and his colleagues in Standard Telecommunication Laboratories Ltd. first introduced the concept of guiding light with optical fibers [4]. Later, since the inception of optical fiber communications, optical fibers, which are glass or plastic cylindrical waveguides that carry light along their length, are irreplaceable in many communications systems all over the world. In addition, over the past 40 years, the

optoelectronics industry has led to the emergence of many new product areas, including compact disc players, personal copiers, and laser printers, etc., due to both the quality improvements and cost reductions in optoelectronic components [5].

Optical fiber sensor (OFS) technology has been a major user of the technology associated with the optoelectronic and fiber optic communications industries. Many of the components associated with these industries were often used for fiber optic sensor applications [6-10]. OFS has been widely used in many different sectors due to its ability of sensing important parameters such as temperature, strain, stress, curvature, vibration, refractive index, position etc. A large number of optical fiber sensors with a variety of functions based on different structures have been reported in recent years, for example, fiber Bragg grating (FBG), tilted FBG (TFBG), long period grating (LPG), taper fibers, core diameter mismatch (CDM) structures and optical fiber balloon structures [6-9],[11]. Displacement and temperature are significant parameters for various applications, ranging from movement monitoring to industrial manufacture, machinery manufacturing and civil engineering [7-9].

Optical fiber sensors have great potential since they could be made with a miniature size, which would help them to be used in many medical applications, especially in the development of minimally invasive surgical tools. Although the penetration into the medical market is slow because of high cost, an increasing number of medical procedures are benefiting from the advantages that these tiny sensors can bring. An example of a medical application is a miniature pressure sensor, which can be used in neurology for intracranial pressure monitoring [10]. Although most high-volume medical applications for optical fiber sensors involve measuring physical parameters, chemical sensing is also a growing market. For example, optical fiber sensors that could detect dissolved oxygen and carbon dioxide or pH are now commercially available [12]. Moreover, since optical fiber sensors are immune to electromagnetic interference, they are perfectly suitable for applications involving high electromagnetic field, such as in magnetic resonance-imaging systems. A fiber optic pH sensor [13] and a fiber optic oxygen sensor [14] have been developed for use in medical applications.

Salinity is an important property of natural and industrial water bodies as physical properties of water changes with salinity level. Salinity measurement is important because a high concentration of dissolved salt in water affects agriculture, drinking

water supplies and ecosystem health. The overall impact of salinity can be extremely costly. Due to such reasons, salinity is a factor of considerable importance in many areas such as in marine environment monitoring, detection of salt water intrusion in drinking water, process control in manufacturing industries, seasonal climate prediction, offshore oil exploration, military engineering and solar engineering [11].

Fundamentally, an OFS works by modulating one or more properties of the propagating light wave, including intensity, phase, polarization, and frequency, in response to the environmental parameter being measured. At the core of the optical sensing technology is the optical fiber that transmits light within its core. An optical fiber is composed of three main components: the core, the cladding, and the buffer coating as shown in figure 1. The cladding reflects light back into the core, ensuring the transmission of light through the core with minimal loss. This is achieved with a higher refractive index in the core relative to the cladding, causing total internal reflection of the light. The outer buffer coating serves to protect the fiber from external conditions and physical damage [5].

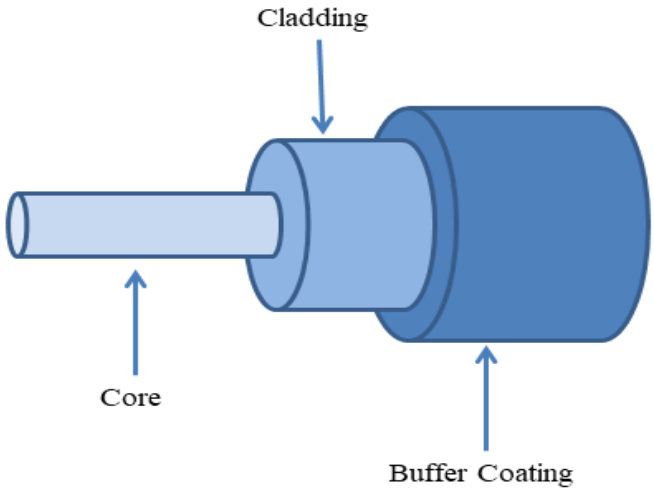


Figure 1 – Typical optical fiber cable.

Source: The author

Optical fiber sensors have been studied intensively based on the physical phenomena such as wavelength dependent absorption, photoluminescence and phase detection. Compared with traditional sensors using electrical or magnetic principles, optical fiber sensors have several advantages, including [5], [6], [9]:

- Low signal loss

- Immunity to electromagnetic noise and chemical material erosion
- Small size and lightweight
- Possibility of multiplexing
- Feasibility of distributed and remote sensing
- Electrical passivity
- Resistance to high temperature

The working principle of OFSs is based on the modulation of the fiber-guided light produced in one of its optical properties by the parameter under investigation. The complexity of the electro-optical system, the type of components selected, and thus cost of the sensor is related to its operating principle [5]. The general structure of an optical fiber sensor system is shown in figure 2. Basically, optical fiber sensors consist of four major components: optical source (Laser, LED, ASE etc.), signal waveguide (e.g., optical fiber), sensing head, and detector. Light propagates along an optical fiber passing through the sensing head, where certain properties of the light wave would be modulated when the sensing head is influenced by the external variations which need to be monitored. The modulated light wave (containing the information) is then received by the detector, and after the demodulation, the external varying parameters which need to be measured could be obtained [5].

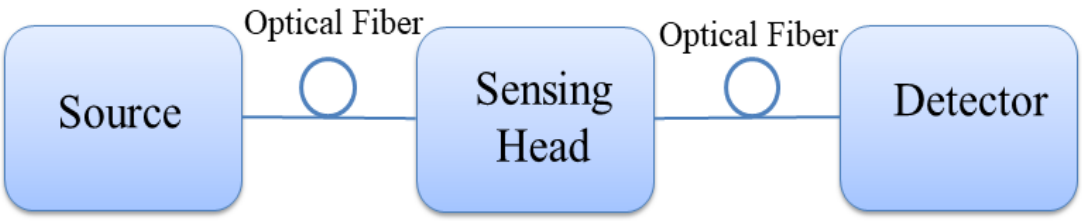


Figure 2 – Basic components of an optical fiber sensor

Source: The author

1.1.1 – Classification of Optical Fiber Sensors

There are a variety of optical fiber sensors. These can be classified as follows:

-- Based on the modulation and demodulation process a sensor can be called as

intensity (amplitude), phase, frequency, or polarization sensor. Since detection of phase or frequency in optics calls for interferometric techniques, the latter is also termed as an interferometric sensor [5, 7].

-- Fiber optic sensors can also be classified on the basis of their application: physical sensors (e.g. measurement of temperature, stress, etc); chemical sensors (e.g. measurement of pH content, gas analysis, spectroscopic studies, etc.); biomedical sensors (inserted via catheters or endoscopes for measuring blood flow, glucose content and so on). Both the intensity types and the interferometric types of sensors can be considered in any of the above applications [9,10].

-- Optical fiber sensors can also be classified in response to their measurements points. The three most important classes are: point to point sensors, multiplexed sensors and distributed sensors. In point to point type there is a single measurement point at a specific point of the optical fiber cable, similarly to most electrical sensors. Multiplexed sensors allow the measurement at multiple points along a single fiber line and distributed sensors are able to sense at any point along a single fiber line, typically every meter over many kilometers of length [9].

-- Extrinsic and intrinsic sensors are another classification scheme. In Extrinsic optical fiber sensors, the optical signal is injected into the sensing element which transduces the measurand to the optical signal. The input fiber enables the light to reach the sensing element. The output fiber permits the optical signal to be injected to the detector where it will be analyzed. Therefore, extrinsic optical fiber sensors use the optical fiber to send light to the transducer and collect it from the transducer. An extrinsic optical fiber sensor is shown in figure 3. A major benefit of extrinsic sensors is their ability to reach places that are otherwise inaccessible [5].

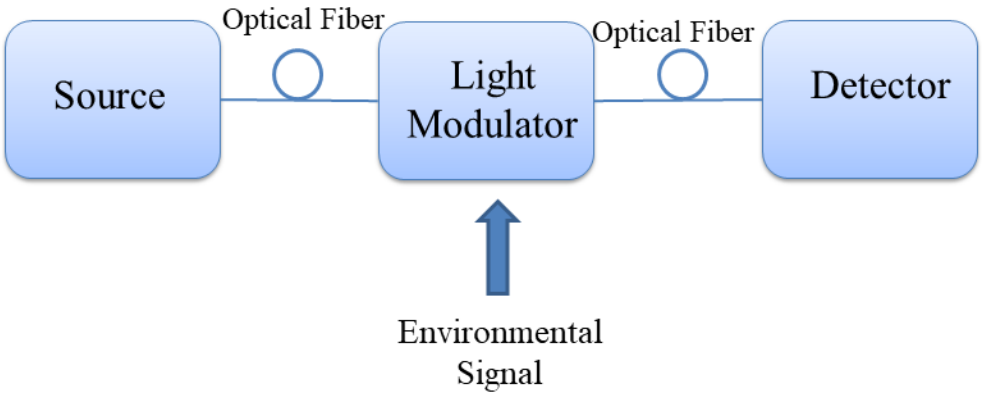


Figure 3 – An extrinsic optical fiber sensor

Source: The author

In intrinsic sensors the optical fiber is the device which will be in contact with the measurand. It is possible to measure strain, temperature, pressure, and other quantities by modifying the optical beam so that the quantity to be measured modulates the intensity, phase, polarization, wavelength, or transit time of light in the fiber. An example of an intrinsic optical fiber sensor is illustrated in figure 4. Sensors that vary the intensity of light are the simplest, since only a simple source and a detector are required besides the optical fiber, for the measurement. A particularly useful feature of intrinsic optical fiber sensors is that they enable distribute sensing over very long distances [5].

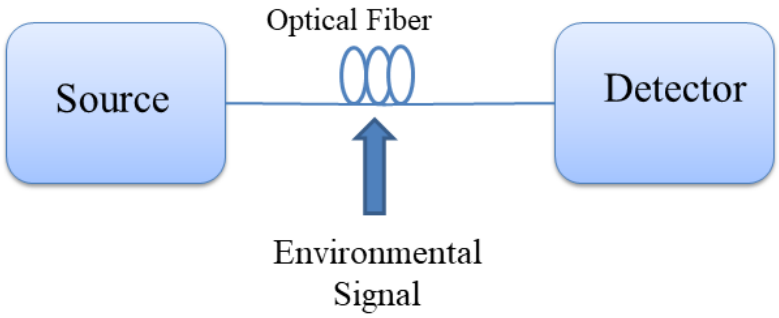


Figure 4 – An intrinsic optical fiber sensor

Source: The author

1.2 – Motivation

Following the fast development of the optical fiber sensor technology in recent years, many kinds of optical fiber sensors have been designed and developed to measure various parameters. To date, a huge number of different parameters could be measured or monitored by optical fiber sensors, such as acceleration, electric and magnetic fields, temperature, pressure, acoustics, vibration, strain, humidity, viscosity, refractive index, etc [15-22]. Optical fiber sensors have become more and more important, and in many industries, they gradually become indispensable, such as in civil, medical, and military applications [23, 24, 25].

Optical fiber sensors could also find helpful applications such as to check pipeline integrity [26], to detect pipeline buckling [27], to detect wall-thinning defects [28], or pipeline leaks [29]. A practical pipeline leakage system [30] with optical fiber sensor for testing is depicted in figure 5. Pipelines provide one of the safest and most reliable approaches for transportation of gases and liquids; however, pipeline failures would cost millions of dollars losses and may have a severe effect on surrounding environment. Hence, monitoring the integrity and health of the pipelines is very important for pipeline industries all over the world. For example, Italy researchers have shown that optical fiber sensors can be used to monitor the structural integrity of a pipeline, and the deformations of the rock or soil surrounding the pipeline [31]. They could measure the amount of pipeline dislocation and its direction by measuring normal strain using stimulated Brillouin scattering along three longitudinal directions running down the pipeline [31]. OFS are expected to play a very important role in the pipeline industries to save money for inspection and maintenance [30].



Figure 5 –Fiber optic sensor for pipeline application.

Source: F. Tanimola [30]

The health of some massive structures, such as aircrafts, wind-turbine blades, bridges, dams, etc., needs to be monitored in a continuous manner to avoid some disaster accidents. For example, researchers in Germany have tested optical fiber sensors based on Bragg gratings in the tail of the Airbus A340/600 which are now converted to cargo, and Airbus was also investigating the use of optical fiber sensors on the A380 [32]. Embedded into the structure of the aircraft, optical fiber sensors which could measure strain offer the aerospace industry with the opportunity to schedule inspection, service and retirement of the aircraft based on the actual loads experienced by the structure. Another example where optical fiber sensors are playing a valuable role is wind-turbine blade [33] shown in figure 6, since the wind turbines become larger and larger which might bring many new engineering challenges. Optical fiber sensors could provide an understanding of real-time loads and blade history that is very important to both the manufacturers and wind-farm owners [33].



Figure 6 – Fiber optical sensor for wind turbine application.

Source: M. Jones [33]

Optical fiber sensors have a potential that they could be made with a miniature size, which would help them be used in many medical applications, especially in the development of minimally invasive surgical tools. An increasing number of medical procedures are benefiting from the advantages of these tiny sensors. OFS can be positioned at the tip of instrumented catheters to give useful feedback in surgical procedures [34]. In figure 7 an endoscopic instrument is presented. This instrument is able to provide the surgeon with haptic information of the type of tissue that may be a vein or a tumor.

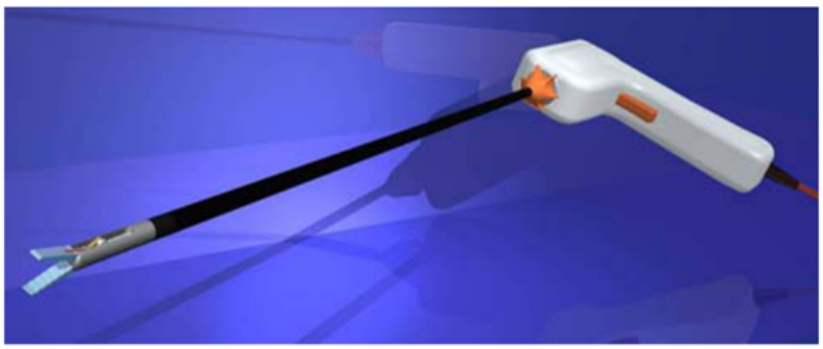


Figure 7– Surgical endoscopic instrument with an optical fiber sensor [34]

Source: J. A. C. Heijmans [34]

Optical fiber biosensors are also very attractive in medical applications, by

measuring absorbance, reflectance, fluorescence, etc., to sense a biological species of interest [35]. For example, the simplest optical biosensors use absorbance measurements to determine any changes in the concentration of analytes that absorb a given wavelength of light. A fiber optic pH sensor [36] and a fiber optic oxygen sensor [37] have been developed for use in medical applications. In addition, Piunno et al. [38, 39] reported one of the first biosensors for direct analysis of DNA hybridization by use of an optical fiber, and researchers in Virginia Institute and State University developed a microgap fiber multicavity Fabry-Perot sensor for biosensing [40].

Salinity plays an important role in chemical and biological analysis, manufacturing process control and protection of ecosystems. Salinity is not only a fundamental parameter for seawater but also an important factor for the monitoring of water quality. Therefore, measurement of salinity has its significance in many fields such as ocean dynamics, marine environment monitoring, weather and climate prediction, agriculture, protection of freshwater resources, and so on [41, 42]. Salinity measurement has a long history [43]. Several emerging sensor systems have been developed for NaCl detection. One of the common methods involved in NaCl detection is based on refractive index (RI) measurement [44]. Measurement of salinity by using optical fiber technology has attracted lots of attentions in recent years due to the well-known advantages of optical fiber sensors. Some researchers studied on the simultaneous measurement of two different parameters [45-51]. In simultaneous measurement, the designing of a dual parameter sensor possesses many advantages such as simple, low cost, compact and conventional operation. It can also be used in many applications such as medical, chemical, environmental assessments, biochemical analysis. In this work simultaneous measurement of salinity and temperature is performed utilizing the balloon shaped structure together with different CDM structures.

1.3– Objectives

The general objective of this work is to develop a fiber-based sensor for simultaneous measurement of temperature and salinity. As specific objectives, the work

searches for new configurations of fiber sensing devices for these simultaneous measurements. Two kinds of fiber structures were analyzed in this work: core diameter mismatch (CDM) structures and the balloon shaped structure.

In a CDM based optical sensor, the technology investigated is based on the core diameter mismatch technique which uses a singlemode fiber (SMF), a multimode fiber (MMF) and a singlemode fiber known as singlemode-multimode-singlemode (SMS) structure. Variations on the SMS structure, such as singlemode-multimode-singlemode-multimode-singlemode (SMSMS), singlemode-mutimode1-multimode2-singlemode (SM1M2S), singlemode-multimode1-singlemode-multimode2-singlemode (SM1SM2S) structures will also be analyzed, where multimode1 and multimode 2 refer to multimode fibers with different diameters.

The other structure, the balloon shaped structure, is formed by bending a singlemode fiber into a balloon shape and will be also verified.

The balloon shaped sensor combined with the SMS structure and its variations will be evaluated as well. The different configurations will be experimentally analyzed as salinity and temperature simultaneous sensor and their sensitivities will be calculated.

The CDM structures will also be simulated on the Beam Propagation software. Comparison of simulation and experimental results will be analyzed.

1.4 – Organization of the Thesis

This thesis is divided in four different chapters. Following this introduction to the research subject, chapter two is a detailed theoretical study of core diameter mismatch structures, balloon shaped structure and multimode interference is presented. In addition to that theoretical concept of different types of CDM structures, the reimaging concept is depicted. A description of the Beam Propagation software is included. In chapter three, experimental details are described, which includes material details, sensor fabrication, the methodology used, and the experimental setup is exhibited. The experimental results of the CDM structures working as sensors are also explained, followed by the simulation results of the same structures. Also in this chapter, the

experiments concerning the balloon shaped sensor are presented. Finally in this chapter, the results from the temperature and salinity simultaneous measurements which used both CDM and balloon structures are showed and discussed. The comparison between experimental and simulation results are also depicted. Finally, the experimental results are compared with other works previous reported in the literature. In chapter four the conclusions arising from the results of the present study are summarized. Suggestions for future work are presented in detail, as well.

2 – Theoretical Analysis

This chapter describes the fundamentals of multimode interference, the conceptual basis of Core diameter mismatch (CDM) structures, the principle of reimaging, and presents some CDM structures. The balloon structure is also explained. Finally, the Beam Propagation Method is explicated since it was used in the simulations presented in this work.

2.1 – Multimode Interference

The phenomenon of multimodal interference and the formation of reimages are known since the early 1990s [52] and have been extensively explored in the manufacture of sensor devices using planar waveguides [53] and optical fibers, in addition to be used in many other devices, such as modulators [54], filters [55] and signal splitters [52]. The injection of light on a multimode waveguide causes the energy of the source to excite several of the many modes of propagation. Along the propagation direction the different modes interfere mutually in sequences of constructive and destructive contributions forming an interference pattern that depends on the geometry of the waveguide, the refractive indexes of the core and the cladding, the dimensions of both and the wavelength used [56] - [60]. Mode interference involving more than two modes results in a spectral transfer function that is not cosine-sinusoidal but instead shows strong peaks at specific wavelengths [61]. This approach is commonly treated as multimode interference (MMI).

MMI fiber devices are typically obtained, by splicing a Multimode fiber (MMF) section between two Singlemode fibers (SMFs), thus forming a Singlemode fiber – Multimode fiber – Singlemode fiber (SMS) structure [53] as shown in figure 8(a), or by splicing an SMF section between two MMFs. In the case of a SMS structure, the length of the MMF section determines the spectral characteristics of the MMI device [53]. The spectral distribution of the transmitted power is highly sensitive to the length of the optical path in the MMF section. The propagation profile diagram along the fiber axis

can be seen in figure 8(b). In figure 8(c) the transmission along the fiber axis is shown, where reimaging is depicted with the red mark circle, as well. Reimaging will be discussed in detail in the next section of this chapter.

In addition to the MMI principle, it is also possible to have a sensor of the same configuration where the coupling is not selective in terms of wavelength, i.e. it is independent on the wavelength [62, 63, 64]. In this case, the SMS device does not act as an MMI device, because the physical length of the MMF is very small (much smaller than the reimaging point, which is the point where the constructive interference between the modes is maximal) and thus the loss in the optical signal increases when disturbed, which makes it attractive for various applications [64][65]. In this sense, for example, attenuation of the optical signal varies when the fiber is subjected to curvature.

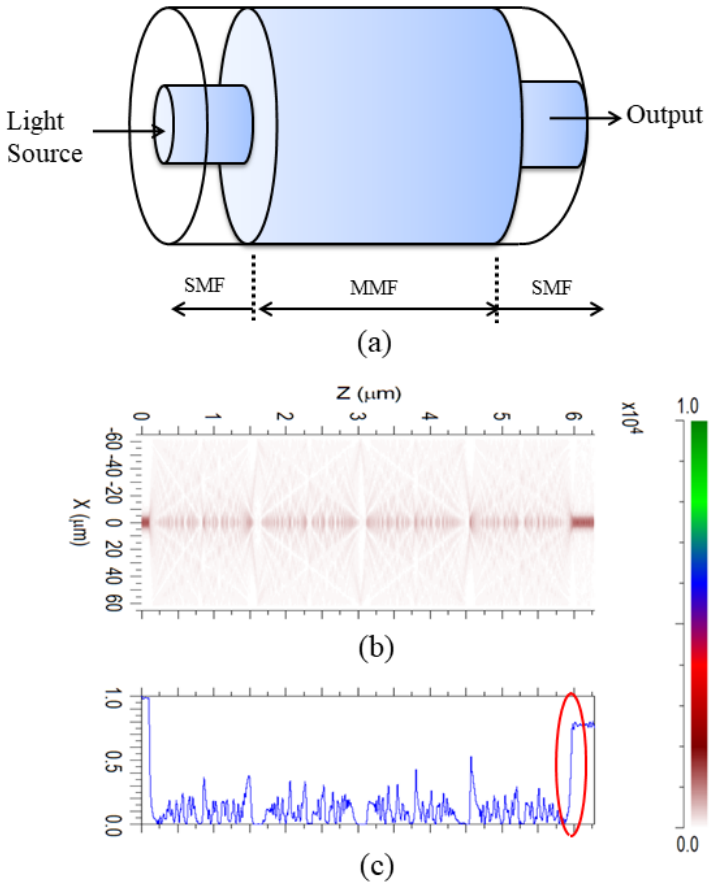


Figure 8 – (a) SMS structure, (b) propagation profile diagram, (c) transmission along the z axis.

Source: The author

Multimode Interference in the multimode fiber section leads to the formation of a reimage of the input singlemode excitation [53]. The main indicator for external perturbations that affects the light consists of the spectral displacement of the reimaging in the multimodal region [17] or the change in the intensity of the transmitted signal.

2.2 – Reimaging

Reimaging of periodic objects was first described more than 150 years ago as cited by [53]. Self-focusing (graded index) waveguides can also produce periodic real images of an object [66]. However, the possibility of achieving reimaging in uniform index slab waveguides was first suggested by Bryngdahl [63] and explained in more detail by Ulrich [67, 68]. The principle can be stated as follows: reimaging is a property of waveguides operating in the multimode conditions where an input field profile is reproduced in single or multiple images at periodic intervals along the propagation direction of the guide [62]. The reimaging distance is obtained where the input source is replicated in both amplitude and phase. An example of reimaging in SMS structure is depicted in figure 9. Figure 9(a) shows the propagation field along the fiber axis and in figure 9(b) reimaging can be observed as indicated by the red circle. The reimaging occurs at 5.8 cm for this example. In this case, the fiber used is a no core fiber with a diameter of 125 μm.

Upon excitation of a multimode waveguide, several modes are excited with different modal propagation constants β_n, where n is an integer mode index. There are usually [59] two consecutive modes that are most excited, with propagation constants β_m and β_{m+1}. A beating phenomenon which appears at propagation distances L_p, is given by [69]:

$$(\beta_m - \beta_{m+1})L_p = 2p\pi \quad (1)$$

with p being an integer number.

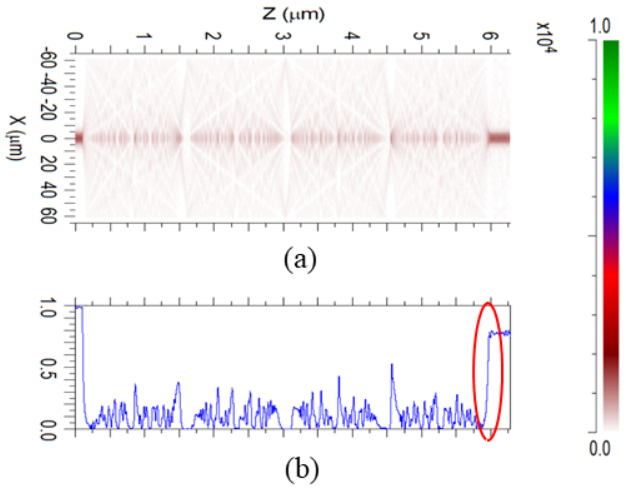


Figure 9 – (a) Field profile within the multimode waveguide showing (b) self-imaging of the input field.
Source: The author

The difference in the propagation constants between the m_{th} mode and other modes is generally different but at some distances it is possible to obtain [69]:

$$(\beta_m - \beta_n)L_q = 2q\pi \tag{2}$$

where q is an integer number that generally differs for each mode n. If $L_p = L_q$ for a group of modes, then a reimage is formed at the distance L_i [69]:

$$L_i = \frac{2p\pi}{(\beta_m - \beta_{m+1})} = \frac{2q\pi}{(\beta_m - \beta_n)} \tag{3}$$

in which the participating modes are the modes satisfying the condition for reimaging [69]:

$$\frac{(\beta_m - \beta_n)}{(\beta_m - \beta_{m+1})} = \frac{q}{p} \tag{4}$$

The reimage distance is then given by [69]:

$$L_i = pL_b = 2p * L_\pi \tag{5}$$

where, $L_b = 2\pi/(\beta_m - \beta_{m+1})$ is known as the beating length of the m_{th} and $(m+1)_{th}$ modes and L_π is their π-length, where the phase difference developed between them is exactly π.

Similar to planar waveguides, optical fibers are expected to have self-imaging characteristics that depend on their graded refractive index profiles. This is well

understood as the modal properties of a multimode fiber depend on its graded profile. A widely used general form of the refractive index profile of weakly guiding optical fibers is given by [69]:

$$n(r) \approx n_{co}\left[1-\left(\frac{n_{co}^2-n_{cl}^2}{n_{co}^2}\right)\left(\frac{r}{a}\right)^{\alpha}\right]^{\frac{1}{2}} ; 0 \le r \le a$$
$$n(r) = n_{cl} \ ; \qquad r \ge a \qquad (6)$$

where n_{co} is the refractive index of the core, n_{cl} is the refractive index of the cladding, r is the radial distance, a is the core radius of the fiber and α is the power of the index graded profile. Two cases of practical interest given by this graded profile are the parabolic-index profile, where α = 2, and the step-index profile where α tends to infinity. For these two cases, approximate analytical forms of the modal propagation constants of a multimode fiber can be used to describe its reimaging characteristics as follows [69]:

2.2.1– Parabolic-Index Fibers

For perfectly symmetric excitations of optical fibers, it can be assumed that fiber modes with axial symmetry and propagation constants β_{0n} are the only ones excited [69]. For graded-index fibers with parabolic index profile, the axially symmetric modes can be approximated by those of an infinite parabolic circular guide, with nearly uniform spacing between their propagation constants [69]:

$$\beta_{0m}-\beta_{0n} \approx \frac{\sqrt{n_0^2-n_{cl}^2}}{n_0 a} 2(n-m)\left[1+\frac{\sqrt{n_0^2-n_{cl}^2}}{2\pi n_0^2 a}\lambda(n+m+1)\right] \qquad (7)$$

$$\beta_{0m}-\beta_{0m+1} \approx \frac{\sqrt{n_0^2-n_{cl}^2}}{n_0 a} 2\left[1+\frac{\sqrt{n_0^2-n_{cl}^2}}{2\pi n_0^2 a}\lambda(2m+2)\right] \qquad (8)$$

where n_0 is the refractive index at the core axis, n_{cl} is the cladding refractive index, a is the fiber core radius and λ is the wavelength. Ignoring the second term in the square brackets, which is a second order term, the reimaging condition approximately holds for

all axial modes as [69]:

$$\frac{(\beta_{0m}-\beta_{0n})}{(\beta_{0m}-\beta_{0m+1})} \approx (n-m) = q \quad (9)$$

The multimode interference pattern appears like two modes interference [52, 53], with reimaging at the position [69]:

$$L_i = L_b = \pi \frac{n_0 a}{\sqrt{n_0^2 - n_{cl}^2}} \quad (10)$$

The second order term would result in small periodic deviations from the ideal wavelength-independent reimaging described by (12) and (13), and gives a slowly beating transmission spectrum with a wavelength period [69]:

$$\Delta\lambda \approx \pi^2 n_0^3 a^2/(m+1)(n_0^2 - n_{cl}^2)L \quad (11)$$

where n_0 is the refractive index at the core axis, n_{cl} is the cladding refractive index, and a is the fiber core radius. L is the length of the fiber. Since all the excited modes of a parabolic index multimode section approximately satisfy the reimaging condition, the transmission of an SMS structure using these graded fibers have maximum values very near to unity [69]. Despite showing this theory, this type of fiber will not be used in this work. But this theory could help in future work.

2.2.2 – Step Index Fiber

For symmetric excitations of weakly guiding step index fibers, the linearly polarized LP_{0n} modes are the only ones excited [53]. For these modes, there is the approximation [70]:

$$\beta_{0m} - \beta_{0n} \approx (\pi\lambda/8n_{core}a^2)[2(n^2 - m^2) + (m-n)] \quad (12)$$

$$\beta_{0m} - \beta_{0m+1} \approx (\pi\lambda/8n_{core}a^2)(4m+1) \quad (13)$$

where, n_{core} is the refractive index of the fiber core, a is its radius and λ is the wavelength. Thus,

$$\frac{(\beta_{0m}-\beta_{0n})}{(\beta_{0m}-\beta_{0m+1})} \approx \frac{[2(n^2-m^2)+(m-n)]}{(4m+1)} \quad (14)$$

Hence, reimaging appears at distance [69]:

$$L_i = 16\, n_{core} a^2 p/(4m+1)\lambda \quad (15)$$

Where p is an integer.

Assuming that $p = 1$ and $m = 0$, field distribution at the input of the MMF is reproduced and is obtained at:

$$L_i = 16\, n_{core} a^2/\lambda \quad (16)$$

2.3 – Core Diameter Mismatch

Core diameter mismatch (CDM) structures offer all-fiber solutions for optical sensing with the advantages of ease fabrication and packaging and connection to optical fiber systems. The CDM structure, generally, works based on the Mach–Zehnder Interferometer. The basic structure of these devices is the Singlemode fiber – Multimode fiber – Singlemode fiber (SMS) which will be analyzed in this chapter. Furthermore, variations on this basic structure can also be good candidates to optical sensors. Some of them, used in this work, will be described in this chapter, as well.

2.3.1 – Singlemode-Multimode-Singlemode structure

The Singlemode-Multimode-Singlemode (SMS) fiber structure is the simplest CDM structure and consists of a short section of multimode fiber (MMF), which works as the

sensing element, inserted between two singlemode fibers (SMFs), as shown in figure 10.

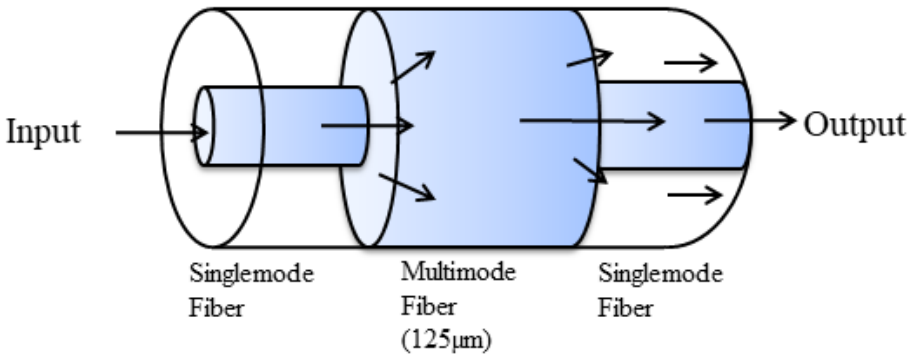


Figure 10 –Singlemode –multimode –singlemode (SMS) structure.

Source: The author

To fabricate this structure, it is only required cleaving and fusion splicing the fibers, a process that is carried out with wide-spread optical fibers equipment. The fibers are cleaved with a high-precision fiber cleaver and are spliced with a fusion splicer machine. A piece of MMF is first spliced to a section of SMF, and then the MMF is cleaved with a length L. Finally, another section of SMF is spliced to the cleaved MMF. The fabrication process is very simple; moreover, it takes a few minutes and is highly repeatable. Note that the structure in which the evanescent fields are accessed is very robust if the outer diameters of the fibers are unaltered [62].

The MMF section acts as a core-cladding coupling mechanism due to the large core diameter mismatch [62]. The MMF couples part of the light traveling along the core of the first SMF to the cladding of the second SMF, and this coupling induces a loss of power in the transmitted signal traveling along the core. The SMS configuration concept is based on the fact that when the light field coming from the first SMF enters the MMF section, it excites several higher order modes, generating a periodic interference pattern along the MMF section. According to the wavelength and geometric length, the light inside the MMF section can interfere in a constructive or destructive way resulting, in the end, in a device with different spectral characteristics [53]. This SMS fiber structure may be used for refractive index, temperature, vibration, curvature and many other parameters sensing. If the MMF is a no core fiber, due to the absence of cladding, the fiber modes are more exposed to the perturbations of the external environment through the evanescent field, therefore, sensing is more effective resulting

in high sensitivity. The role of the SMF is to cast and collect light at the end of the MMF. In figure 11(a) the SMS structure is presented. It was represented in the Beam Prop software where light enters from the singlemode fiber and excites higher order modes in the multimode fiber with destructive and constructive interferences, as presented in figure 11(b), which leads to the reimaging illustrated in figure 11(c) encircled by the red line at the end of the transmission propagation along the fiber axis.

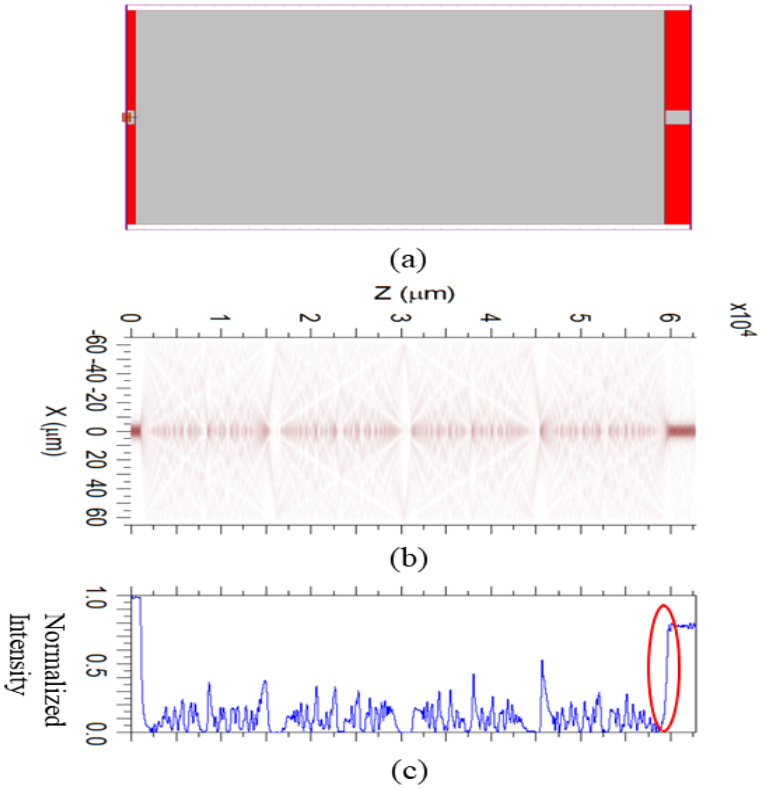


Figure 11 – (a) Beam propagation model of SMS structure, (b) propagation field and (c) transmission along the z axis.

Source: The author

In this work, two different fibers were used as the MMF: the no core fiber which is a rod of silica with a diameter of 125µm, a refractive index of 1.444024 and reimaging is obtained at the length of 5.8cm. The MMF with core/cladding diameters of 105/125µm, core refractive index of 1.457 and cladding refractive index of 1.44 and reimaging is obtained at 4.3cm. The SMF used in this work presents a core refractive index of 1.4492 and a cladding refractive index of 1.444024. Conventional MMF operates similarly to the MMFs used in this work but with less sensitivity due to its smaller core diameter. The reflection occurring at the interface between the singlemode fiber and the multimode fiber due to the mismatch of the refractive index is found to be very small

and can be neglected in practice [56].

2.3.2 – Singlemode-Multimode-Singlemode-Multimode-Singlemode structure

In the Singlemode-Multimode-Singlemode-Multimode-Singlemode (SMSMS) structure depicted in figure 12, when the optical beam outputs the first SMF and enters the first MMF several higher order modes are excited in the MMF section. Thus, the modes further travels to the middle SMF where part of the light leaks from the MMF to the cladding of this SMF due to the different core diameters between the SMF and MMF. After propagating through the second MMF, part of the modes re-couples into the core mode of the last SMF. Once the cladding modes in the middle SMF propagate by the cladding boundary, the middle SMF is more sensitive to the neighboring material [71]. In the case of figure 12, the MMFs are no core fibers such as the one described at the last section.

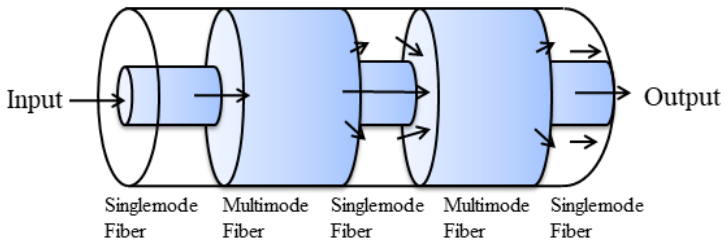


Figure 12 – Singlemode –multimode –singlemode–multimode –singlemode (SMSMS) structure

Source: The author

The effective refractive index of the middle SMF cladding modes is determined by the difference between the refractive index (RI) of the cladding and that of the external medium thus in such cases transmission depends on the refractive index of the external medium. Consequently, the device can be exploited for many sensing applications. The core of the middle SMF, which is not in direct contact with the external medium, also guides some light. This makes the transmission of the device

never to be zero even in the case when the RI of the external medium is higher than that of the cladding. The insertion of the SMF between two MMFs causes losses that are typically below 2-5dB [54, 62].

When light propagates through the MMF and reaches the middle SMF, at the MMF-SMF splice point, part of the power can be coupled to the cladding modes of the middle SMF due to the core diameter mismatch. Generally, the refractive index of the MMF no core is matched with the refractive index of the SMF fiber cladding and along with the large core diameter mismatch guarantee for the excitement of cladding modes at the middle SMF. Similarly, at the middle SMF-MMF splice point, part of the cladding modes of the middle SMF will be again coupled to the guided modes of the MMF, together with the core mode of the middle SMF. Because of the effective refractive index differences between the middle SMF cladding and core modes, an interference pattern could be expected at the end of the structure and can be noticed by measuring the transmission spectrum of the device [54].

Figure 13(a) shows the SMSMS structure represented in the Beam propagation software where the MMF used in the structure is the no core fiber with a diameter of 125μm. In figure 13(b) the propagation of light with constructive and destructive interferences is observed. In figure 13(c) the reimaging for both MMFs is illustrated by the red circles at 5.8 cm length of the fibers.

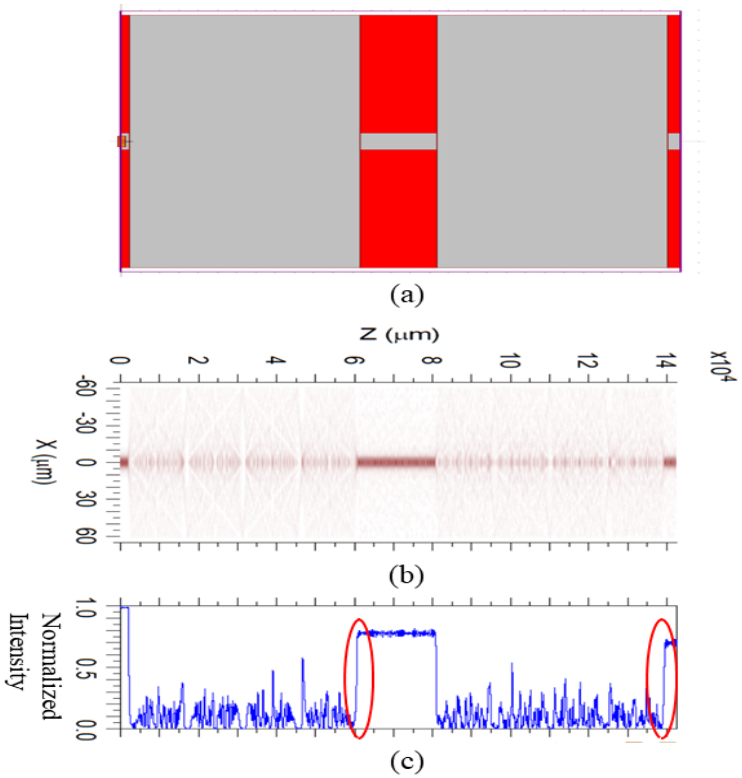


Figure 13 – (a) Model structure of SMSMS, (b) propagation of light and (c) transmission along the z axis

Source: The author

2.3.3 – Singlemode-Multimode1-Singlemode-Multimode2-Singlemode structure

Figure 14 illustrates the Singlemode-Multimode1-Singlemode-Multimode2-Singlemode (SM1SM2S) structure. In this case, the multimode fibers present different diameters, therefore, they are called multimode fiber 1 (Multimode1) and multimode fiber 2 (Multimode2). This device's principle of operation is very similar to the SMSMS structure: Light propagates along the core of the first singlemode fiber as the fundamental core mode. Once the optical beam reaches the interface of the first MMF section numerous modes are excited in this fiber. Once they reach the interface to the middle SMF, part of them propagate in the core of the singlemode fiber as the fundamental mode and the other part travel in the cladding as cladding modes. Further travelling, they reach the interface to the second MMF where part of the cladding modes

is re-coupled into core modes and the others propagate in the cladding of this MMF. Finally, part of the MMF core modes excites the fundamental mode of the last SMF.

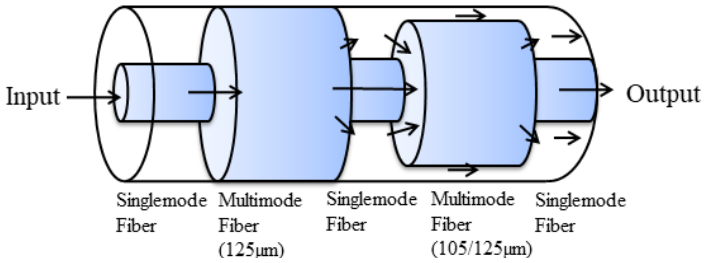


Figure 14 – Singlemode –multimode1 –singlemode–multimode2 –singlemode (SM1SM2S) structure.

Source: The author

Figure 15(a) shows the structure of the SM1SM2S represented in the Beam propagation software where the M1 fiber is the MMF no core fiber with a diameter of 125μm and the M2 fiber is the MMF with core/cladding diameters of 105/125 μm. In figure 15(b), the propagation of light with constructive and destructive interferences is presented. In figure 15(c) the reimaging in red marked circles for both MMFs are depicted at 5.8 cm and 4.3 cm lengths for M1 and M2 fibers, respectively.

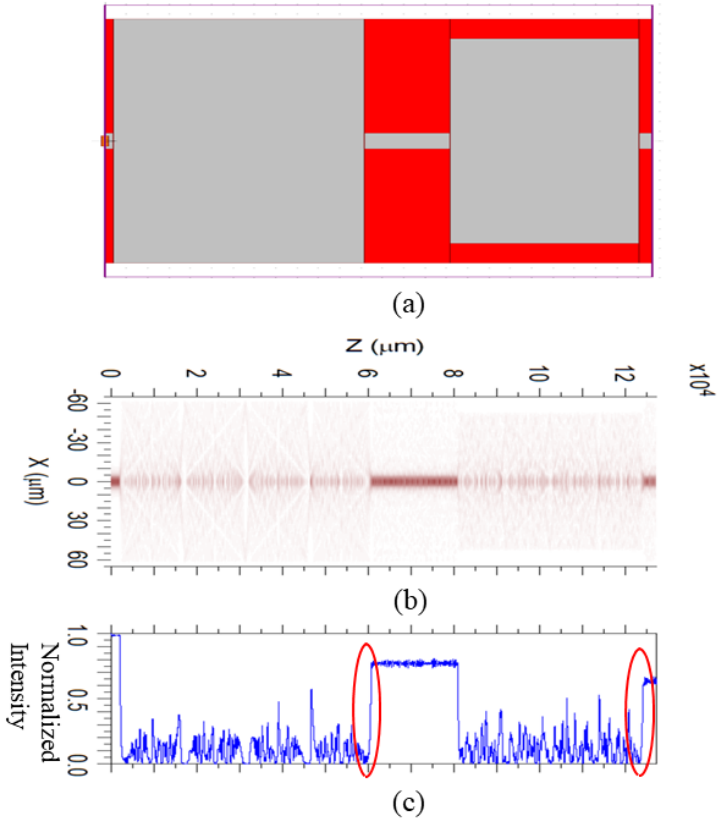


Figure 15– (a) Beam Propagation software model of SM1SM2S structure, (b) propagation, (c) transmission along the z axis.

Source: The author

2.3.4 – Singlemode-Multimode1-Multimode2-Singlemode structure

The schematic diagram of the Singlemode-Multimode1-Multimode2-Singlemode (SM1M2S) structure is illustrated in figure 16. This structure is formed by splicing two multimode fibers with different diameters and each one is spliced to a singlemode fiber. When light propagates from the first SMF section and reaches the first MMF section it excites many higher order modes in this fiber. Light travels along the M1 section and when it reaches the M2 section, part of the light leaks into the cladding of the M2 fiber. Light travels along the last MMF and part of the optical beam enters the last SMF section where light is coupled back from the M2 section with optical power loss due to light leakage from the cladding of this SMF.

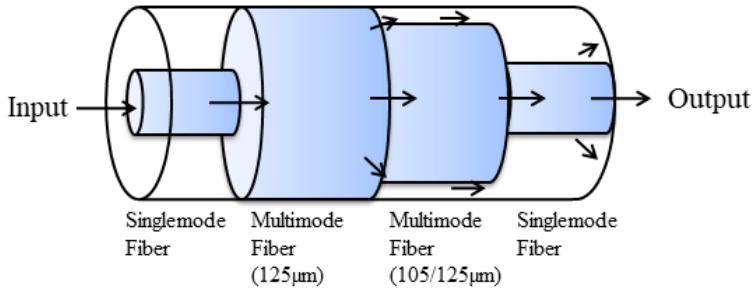


Figure 16 – Singlemode –Multimode1–Multimode2 –Singlemode (SM1M2S) structure.

Source: The author

Figure 17(a) illustrates the structure of the SM1M2S represented in the Beam propagation software. The MMFs used in this structure are the same utilized in the SM1SM2S structure. In figure 17(b) propagation of light with constructive and destructive interferences is presented. In figure 17(c) MMFs reimaging at 5.8 cm and 4.3 cm lengths respectively are shown with the red marked circles.

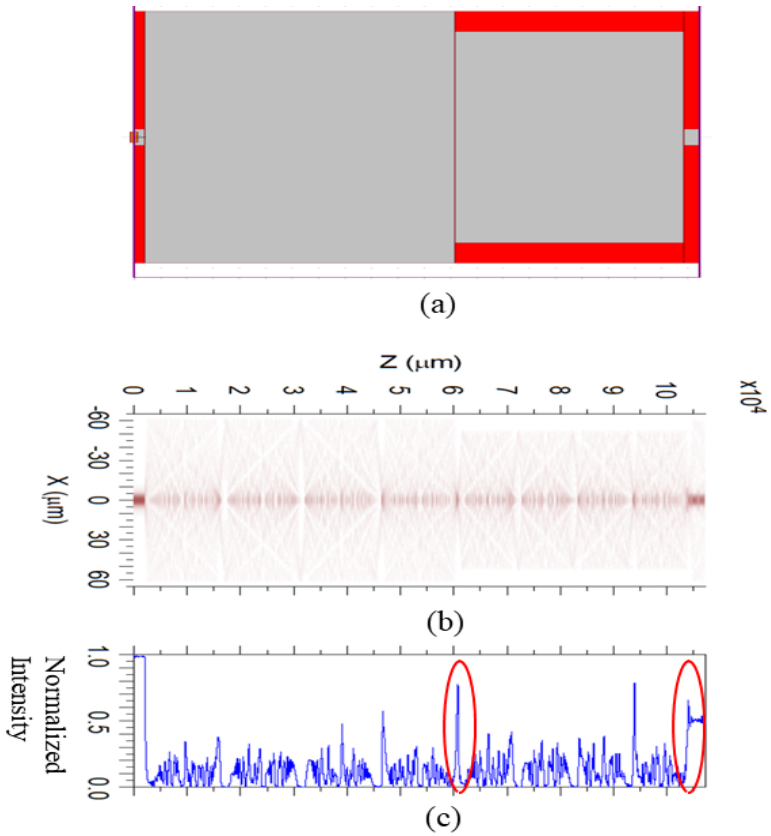


Figure 17 – (a) Model structure of SM1M2S in Beam propagation software, (b) light propagation and (c) transmission along the z axis.

Source: The author

2.4- Balloon Shaped structure

The balloon shaped structure is based on the Mach-Zehnder Interferometer (MZI) configuration assembled with standard singlemode fiber. Light from the source initially propagates along the straight input section of the SMF, as the core fundamental mode, until it reaches the bending portion of the SMF which starts at point A as depicted in figure 18. From point A, part of the optical beam propagates in the cladding of the singlemode fiber, exciting cladding modes that travel in the bending region through the cladding of the singlemode fiber till point B in figure 18, which is the ending part of the bent. From point B onwards, the cladding modes recouple back into the core which results in core and cladding modes interference. Thus, the MZI is produced since there exist two optical paths faced by the optical beams traveling in the core and the cladding of the SMF.

The assembly of the balloon shaped structure is a quite straightforward procedure. Firstly, the coating of a singlemode fiber was stripped of over a length of 3 cm, and both ends of it were input in a capillary cylinder with a length of 1.5 cm and an internal diameter of 1.5 mm. The capillary tube and the balloon shaped sensor are firmly attached by gluing them on a glass slab.

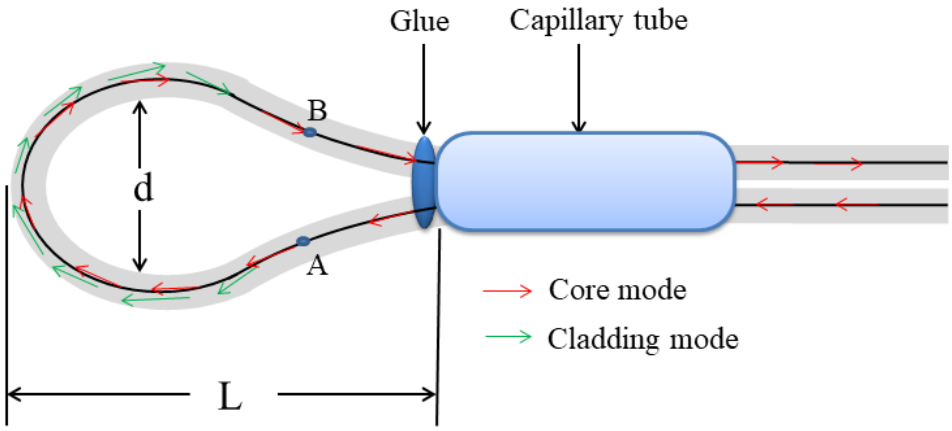


Figure 18 – Schematic diagram of the balloon shaped sensor.

Source: The author

The transmission spectrum (from 1500 to 1630 nm) of the balloon shaped structure for several bending diameters was experimentally obtained and can be observed in figure 19. Once the bending diameter d, of the SMF was superior to 1.37 cm, no interference pattern occurs because little or no optical beam is coupled into the cladding. Then, the bending diameter was reduced from 1.37 cm to 0.78 cm. As the diameter is decreased, the intensity loss of the transmission spectrum enlarges since much of the light is coupled into the fiber cladding causing mode interference. If the bending diameter is decreased further, additional light is coupled into the cladding and may even emerge from the cladding which results in a considerable loss. In this work, 0.94 cm of the bending diameter is used. With the balloon shaped diameter curvature of 0.94 cm, an available interference dip appeared with relatively large extinction ratio (more than 15 dB). When the diameter curvature was changed to 0.87 cm (or even smaller), interference dips were detected, as well. However, when the measurements were performed, no variation in the wavelength or in the optical power was achieved, neither for salinity nor for temperature measurements. It is due to the following: as the bending radius decreases, excess light is coupled into the cladding and can even leak out from the cladding resulting in a large signal loss.

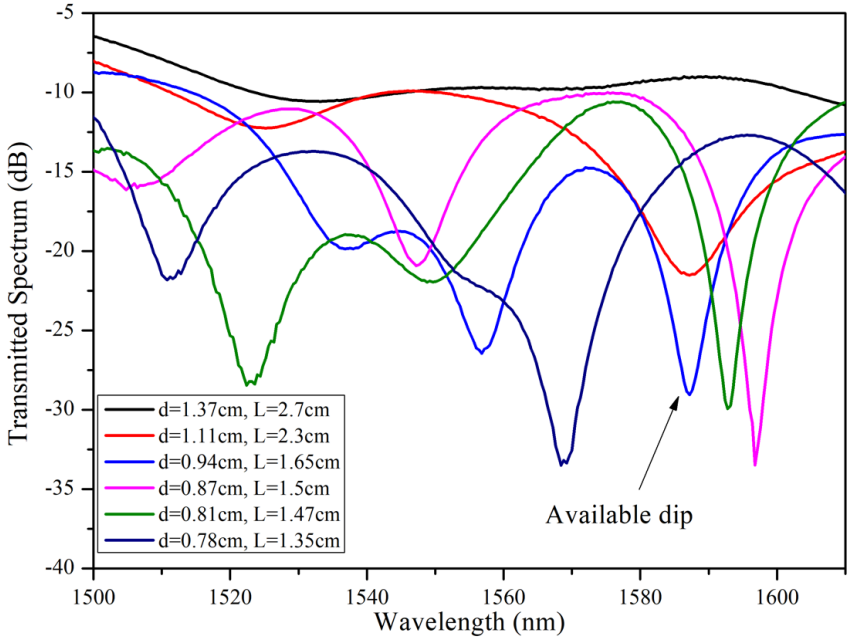


Figure 19 – Transmission spectrum of the balloon shaped structure for different diameters values.

Source: The author

A balloon sensor is a straightforward and stable structure for RI and temperature measurement based on standard singlemode fiber. The device is of easy fabrication, with low cost and high sensitivity.

The bending section of the balloon induces a phase difference (φ) between the core and cladding modes that can be described as [72].

$$\varphi = \frac{2\pi}{\lambda}(n_{co} - n_{cl})L_{eff} \quad (17)$$

Where n_{co} and n_{cl} are the core and cladding modes effective refractive indexes respectively, λ is the wavelength and L_{eff} is the effective length of the bent section of the balloon which allows the transmission of the excited modes.

When the phase difference of the bending section meets the condition of $\varphi = (2k + 1)\pi$, where k is an integer denoting the interference order, a destructive interference occurs and an interference valley (or dip) appears at a specific wavelength that is expressed as [72]

$$\lambda_k = \frac{2(n_{co} - n_{cl})L_{eff}}{(2k+1)} \quad (18)$$

From equation (18) it is clearly noticed that λ_k is directly proportional to the effective bending length L_{eff} and the effective refractive indexes difference between the core and cladding modes. It is important to mention that the effective bending length is not the length of the bent section but it is an effective length that enables the propagation of the excited cladding modes. A larger bending angle of the balloon permits the optical beam to be coupled into the cladding formed in its transmission path and consequently produces a larger propagation length for the excited cladding modes [73]. In a bent device, a larger bending diameter *d* may lead to a larger effective length L_{eff}. However, for the temperature and salinity measurement the effective bending length of the balloon is maintained constant, so the interference dip or valley λ_k is determined based on the difference of the effective refractive indexes of the core and the cladding modes $(n_{co} - n_{cl})$.

2.5 – Beam Propagation Software Method

In this work, the BeamPRO software was used as the simulation tool. It is a design tool of the company Rsoft Group based on the Beam Propagation Method (BPM). It is a widely used tool for the design and simulation of integrated and optical fiber waveguide devices and circuits. BPM allows the modeling of photonic devices such as optical fibers, photonic crystal optical fibers, resonator rings, waveguides and optical integrated circuits among others. In our study, BPM is used to study the propagation of the light in the CDM structures.

BPM calculates the spread of light in different types of geometry, making use of the finite difference method to solve the parabolic or paraxial approximation of the Helmholtz equation [74]

$$\frac{\partial^2 \emptyset}{\partial x^2} + \frac{\partial^2 \emptyset}{\partial y^2} + \frac{\partial^2 \emptyset}{\partial z^2} + k^2(x, y, z)\emptyset = 0 \qquad (19)$$

where, $\emptyset$ is a component of the field and k is the wave number.

The paraxiality condition imposes a propagation limitation restricted to a narrow range of angles. As shown in section 2.3.1, in an SMS structure the largest part of the energy transferred from the singlemode segment to the multimode segment, the coupling occurs to the lower order modes, which are the modes with the highest propagation constants and effective indexes, which validates the condition of the approximation of the applied method. The BPM technique approximates the exact wave equation, using the Helmholtz equation for monochromatic waves, formulating the problem in the form of scalar field [74], which is defined as

$$E(x, y, z, t) = \emptyset(x, y, z)e^{-i\omega t} \qquad (20)$$

where, ω is the angular frequency and the wave number is spatially dependent and defined by [74]

$$k(x, y, z) = k_0 \cdot n(x, y, z) \qquad (21)$$

Where, n (x, y, z) is the refractive index of the medium. The wave number in free space is given by $k_0 = 2\pi / \lambda$.

Thus, the geometric properties of the problem are defined by n (x, y, z). This approach is particularly important in the conformal transformation employed for curvature simulation. The simplifications adopted by this method in the BeamProp program, allow great efficiency with respect to the simulation time, compared to the solution of the complete numerical version of the Helmholtz equation [74]. Another advantage is that the method uses a slow-changing envelope allowing the variant field to be represented numerically on a longitudinal grid along the z axis, which can have elements much larger than the wavelength, which contributes greatly to the efficiency in the simulation [74]. As a disadvantage, the method does not allow simulations with a high rate of variation of refractive index along the z axis [74]. The models analyzed in this work do not present marked variations in the refractive index on the z-axis. The approached structures have longitudinal dimensions much larger than the wavelength, so that the simplification of considering the envelope of the wave (and not their rapid oscillations) is a good approximation.

The flow chart of the BeamProp software is shown in figure 20. To start the program in the BeamProp software it is necessary firstly to choose a new circuit where the basic information about the circuit to be modeled is entered, including the wavelength of the light, the background refractive index, the default index change between the background material and the structure, and the approximate overall dimensions of the device. Using Symbol Table it allows the user to create/modify both built-in and user-defined variables, initializing the variables, for example length of the fiber, refractive indexes of core and cladding, radius of fiber on so on. After initializing the variables, it is possible to start drawing the structure with the help of segment modes which are always selected by default. Length of the structure and other parameters can also be changed after drawing the components. The launch is the components which inject light i.e. optical power through the components of the model. The launch parameters can be changed. Pathway are defined where a launch field is outlined. A pathway is nothing but the path which light had to follow for the simulation through the components. The pathways are used to tell or monitor where to perform computations for the monitor analysis. Pathway monitors allow measurements to be made during a simulation for viewing or processing. Once the layout and analysis setup are complete, the simulation can initiate. After a simulation is initiated, the computation begins in a

new window separated from the main program. The simulation program runs as a background task, so that another program, or back to the main program to edit another structure to begin another simulation is possible. After completion a notification is presented.

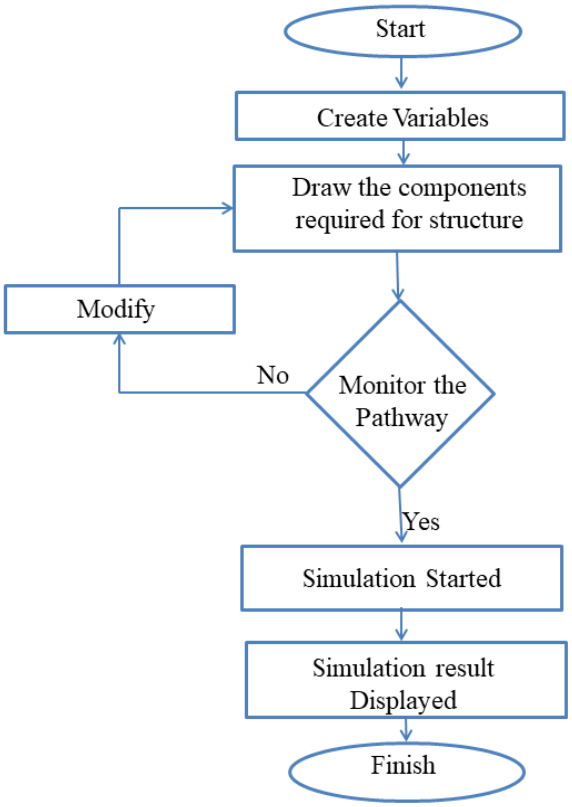


Figure 20 –Flow chart of the Beam Propagation software.

Source: The author

The Beam propagation software outlook is illustrated in figure 21. This is the initial display of the SMS model, as an example. This is a 3D model and can be observed in 4 visions (4P): X, Y, Z and 3D aspect. The SMS Sensor has 6 segments (SMF cladding and core; MMF clad and core; SMF cladding and core) as depicted in the figure 21. In the Reference box you can change the way you define the length. The RI is defined by Index Difference.

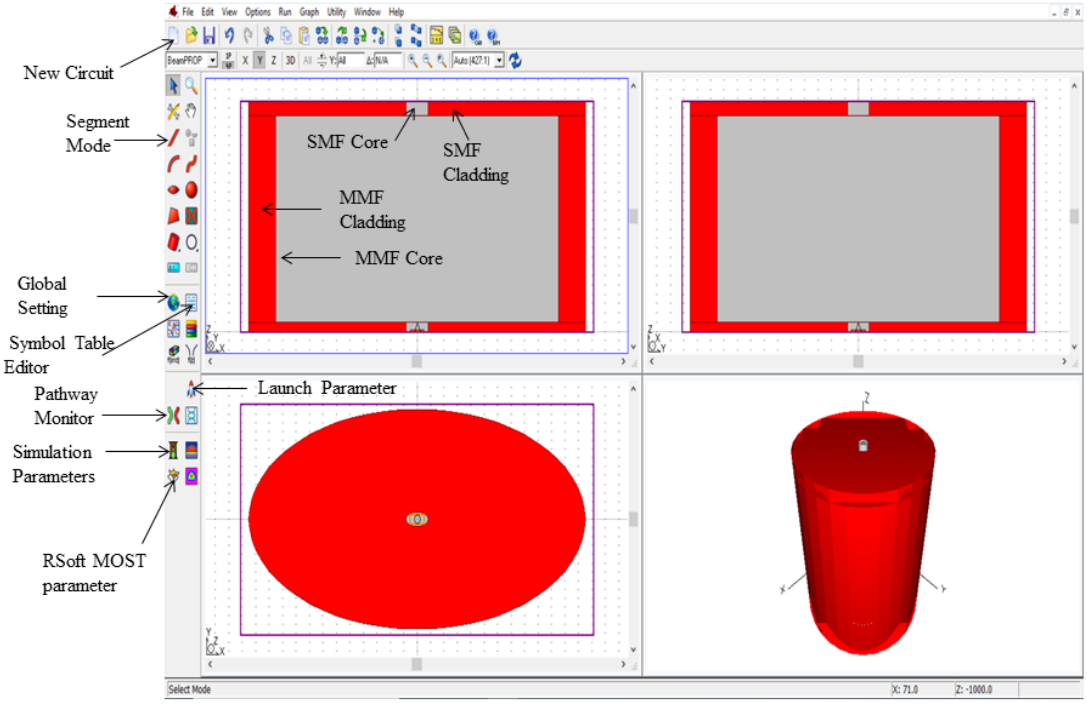


Figure 21 – Outlook of the Beam Propagation Software.

Source: The author

In Global setting option, the parameters can be set such as wavelength, component height, component width, index difference and background refractive index as presented in the figure 22.

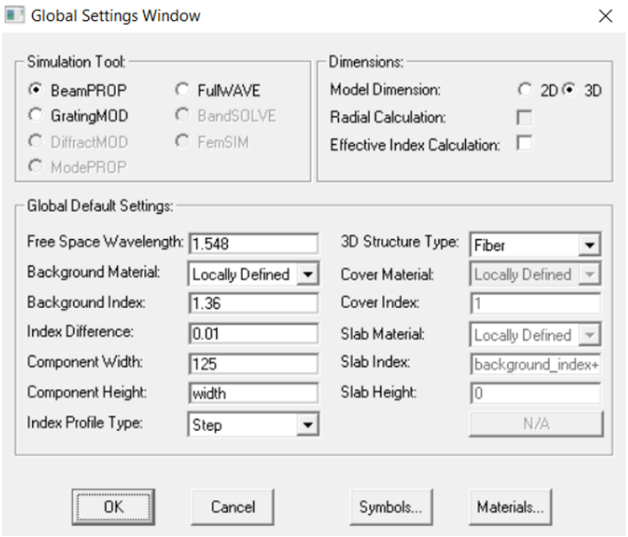


Figure 22 – Global setting window.

Source: BPM Software

In the simulation tool, as shown in figure 23, some parameters can be set such as: the sizes of X, Y and Z, the grid configuration (essential), the display mode (different types of graphics) and so on. In the output prefix the name of the simulation is included. From each window it is often possible to have access to others like, Launch, Symbols, etc. The grid is important, because it sets the size of the elements used to do the simulation. Smaller the grid sizes better the result.

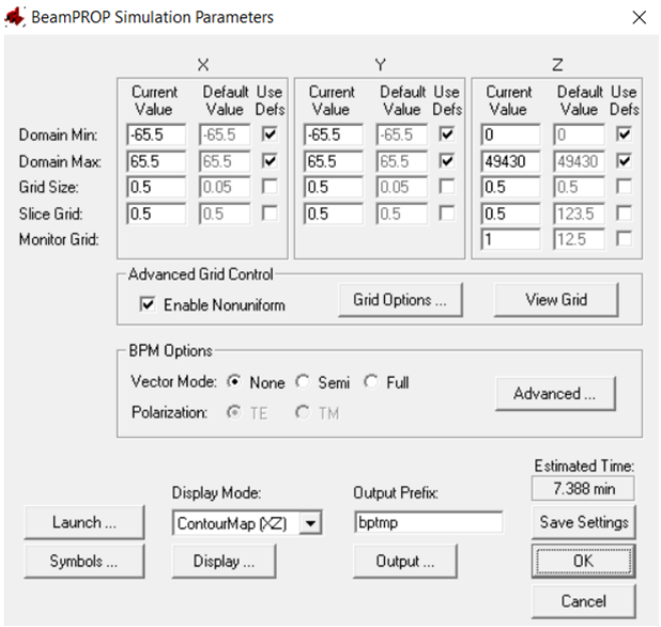


Figure 23 – Simulation Parameter window.

Source: BPM Software

All this information is set as the input for the simulation to obtain the desired output. Output of the simulation shows the interference pattern of the model and the transmission of light in which we can see the reimaging after some interval.

3 – Experimental Measurements and Theoretical modeling

This chapter describes the fabrication process of the CDM and Balloon sensor. Experimental details are also presented about the salinity and temperature measurements individually and simultaneously. Measurement and simulation results are discussed, as well.

3.1 – Sensor Fabrication Process

A simple technique is used to fabricate the sensor. There are three main steps which are included in the fabrication process for the CDM structures. For the balloon shaped structure, only the first two steps are needed (concerning the three steps below).

1. Stripping: Removing the cladding and cleaning the fiber using alcohol solution.
2. Cleaving: Cutting the edge surface of the fiber at 90^0 using a cleaver equipment. This equipment is shown in figure 24(a) with a fiber on it.
3. Fusion process: The fibers that will be spliced are placed in the micro positioner of the splicing machine as shown in figure 24(b). Testing of compatibility, free of foreign objects debris and alignment of the two optical fibers are carried out by the splicing machine. After fusion splicing, the fibers are joined as shown in figure 24(c).



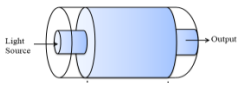
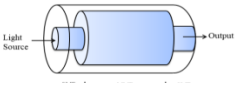
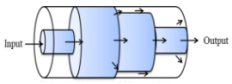
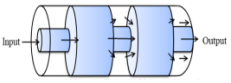
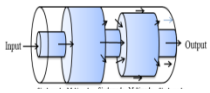
(a) (b) (c)

Figure 24 – a) Cleaver equipment, (b) Fusion machine, (c) Fibers fusion spliced

3.1.1– CDM structures

In all CDM structures, the singlemode fiber used was the Corning SMF-28. Five different types of CDM structures are used in this experimental work, which are described in Chapter 2. Summary of different types of CDM structure is shown in the table 1.

Table 1: Summary of different types of CDM structure

CDM Structure Name	CDM Structure Figure	MMF type	Core diameter (µm)	Cladding diameter (µm)	MMF length (cm)	Middle SMF length (cm)
SM1S		M1 is a no core fiber	----	125	5.8	---
SM2S		M2 is a multimode fiber	105	125	5.8	---
SM1M2S		M1 is a no core fiber	----	125	5.8	---
		M2 is a multimode fiber	105	125	5.8	---
SM1SM1S		M1 is a no core fiber	----	125	5.8	2.0
SM1SM2S		M1 is a no core fiber	----	125	5.8	2.0
		M2 is a multimode fiber	105	125	5.8	

3.1.2. Balloon Shaped Structures

For the fabrication of the balloon shaped structure, beyond the two first steps mentioned in the beginning of section 3.1, some other processes were needed: the coating of the Corning SMF-28 singlemode fiber was stripped of over a length of 3 cm

to form balloon shaped sensor, and both cleaved ends of it were input in a capillary cylinder with a length of 1.5 cm and an internal diameter of 1.5 mm. Capillary tube and the balloon shaped sensor are firmly attached by gluing them on a glass slab. A photo of the Balloon sensor is shown in figure 25. One end of the SMF which will be the input is connected to the CDM structure, and the other end of the SMF that is the output will be directly connected to the OSA.

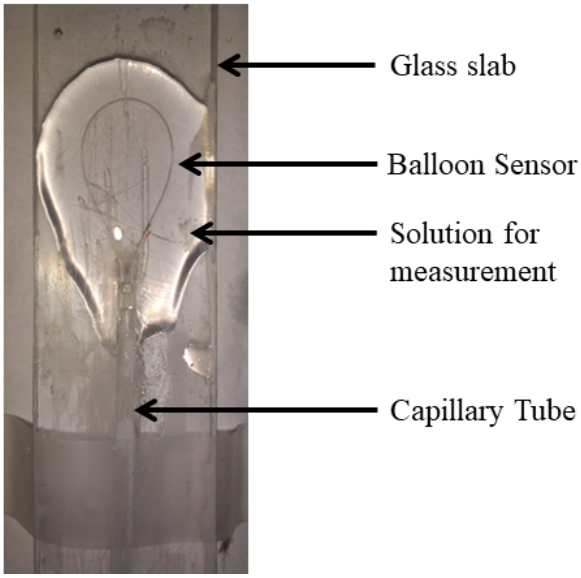


Figure 25 – Photo of the Balloon sensor used for performing the experiments.

3.2. Saline Solution Preparation

The saline solutions are prepared by mixing different quantities of NaCl in 100 ml of water to obtain the different levels of salinity. The saline solutions are prepared with NaCl concentration of 5 to 35 g (in steps of 5 g) per 100 ml of distilled water. The refractive index (RI) of the liquids is directly proportional to the salinity of the water. The sensors are tested for salinity percentage in water varying from 5 to 35% with the respective refractive index ranging from 1.3415 to 1.38 as depicted in table 2. Refractive indexes are measured with an ABBE refractometer.

Table 2: Refractive index with respect to salinity percentage

Salinity (% NaCl)	Refractive Index
5	1.3415
10	1.3495
15	1.3562
20	1.3642
25	1.3713
30	1.3781
35	1.3864

3.3 – Experimental Details

The experiments were conducted for the detection of salinity and temperature in water using CDM and balloon shaped structures. All the experiments were performed at a temperature-controlled laboratory at room temperature. We also covered the laboratory optical table with paper or plastic, so that there was a negligible heat loss. Light from the broadband (Thorlabs Fiber Coupled SLD) source (BBS) is transmitted through the sensors until it reaches the ANRITSU optical spectrum analyzer (OSA) with a resolution of 0.07 nm.

In the measurements using the combination of the Balloon and CDM sensor the light from the BBS is transmitted through the Balloon sensor, after that it passes through the CDM sensor and reaches the OSA. Figure 26 illustrates the measurement configuration.

Figure 27 presents a photo of the experimental setup used at the laboratory for the salinity and temperature measurements of the CDM sensors. Figure 28 depicts the

experimental setup for the combination of Balloon and CDM sensor for the measurement of salinity, temperature, and simultaneous measurement.

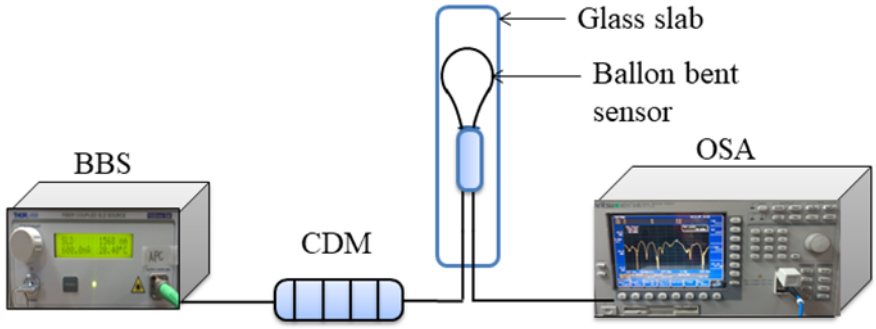


Figure 26 – Schematic diagram of the experimental setup with the combination of the CDM and Balloon shaped sensor.

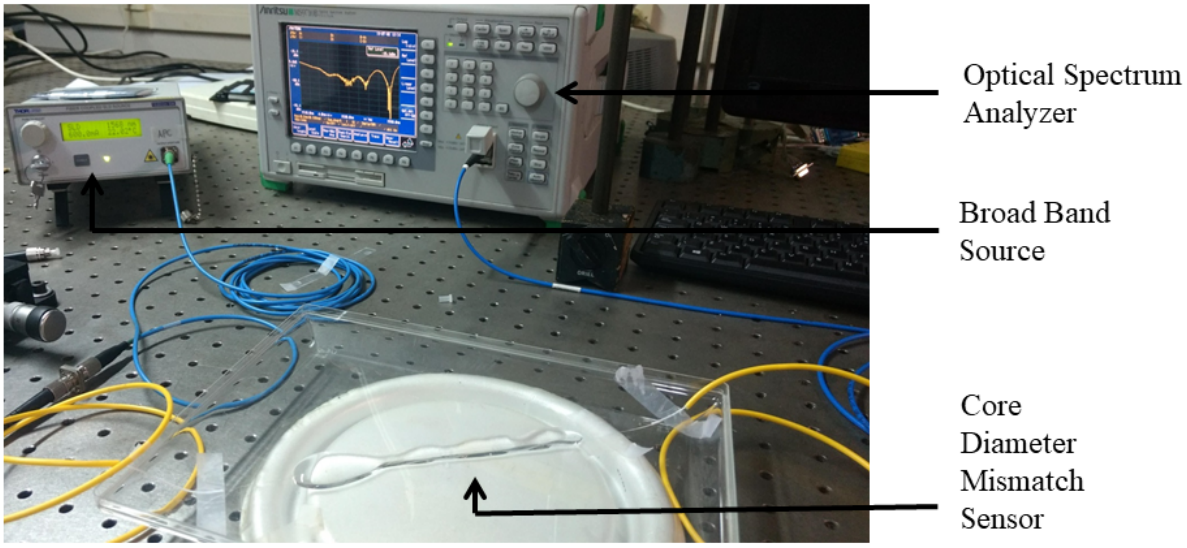


Figure 27 – Experimental setup of the CDM structure sensor for measurement of salinity and temperature.

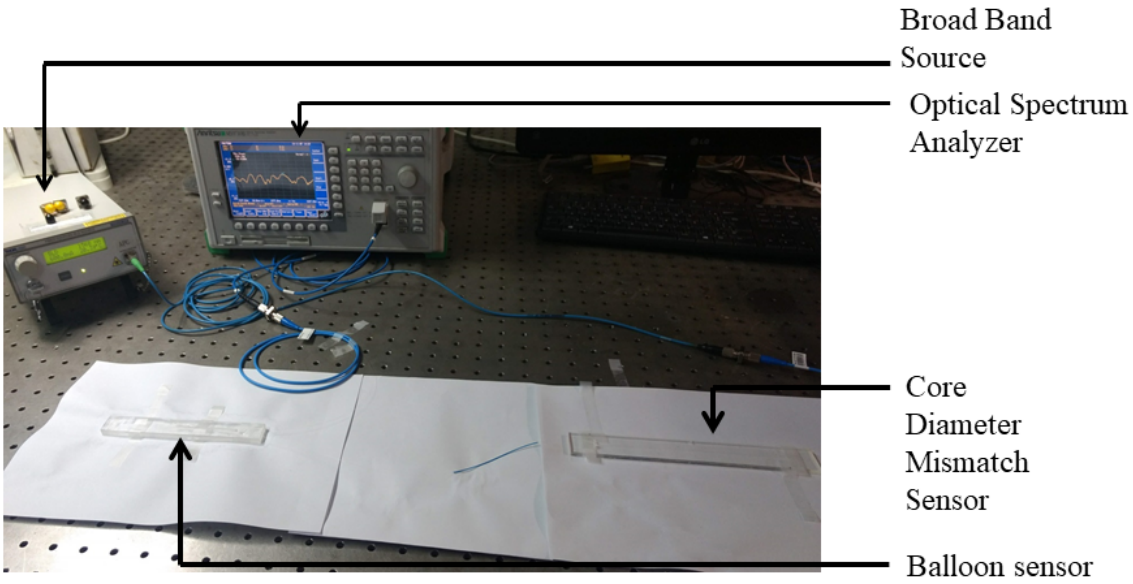


Figure 28 – Experimental setup of the Balloon and CDM sensor for measurement of salinity, temperature and simultaneous measurement.

Three different types of measurement were developed:

(a) Salinity measurement only: (1) Only the CDM structures (SMS, SM1SM1S, SM1SM2S and SM1M2S), (2) the CDM structures (SMS, SM1SM1S, SM1SM2S and SM1M2S) with the balloon shaped structure. In this experiment, all structures are immersed in saline solution with NaCl ranging from 5 to 35%.

(b) Temperature measurement only: (1) Only the CDM structures (SMS, SM1SM1S, SM1SM2S and SM1M2S), (2) the CDM structures (SM1SM1S, SM1SM2S and SM1M2S) with balloon shaped structure. In this case, all structures are submerged in hot purified water whose temperature is varied from 21 to at most 75 °C.

(c) Salinity and temperature simultaneous measurement: the SM1SM2S structure was immersed in distilled water with temperature ranging between 21 and 45 °C and simultaneously the balloon shaped structure was submerged in saline solution with NaCl ranging from 5 to 25%.

For the repeatability of the results, every type of experiment is repeated three times and in some cases five times, as well. The repeatability was checked and confirmed. Sensitivities were obtained for all measurements. However, only the best results are presented here.

3.4 –Results for Salinity Measurement

3.4.1– CDM structures Only

3.4.1.1 – SM1S

The experiment for salinity percentage is performed with the SM1S sensor with the no core multimode fiber. The salinity solutions were prepared by mixing NaCl and water. The refractive index of the salinity solutions ranges from the 1.3415 to 1.386. Figure 29 (a) shows the variation in the spectrum for the different percentage of salinity solutions. The sensitivities were calculated at the two Peaks and one Dip depicted in Figure 29 (a). Dip 1 varies from 1552nm to 1562nm. Figure 29 (b) shows the sensitivity of Dip 1 since it presents the best sensitivity with R^2 equals 0.99. The sensitivity value is 289.3 pm/% of NaCl.

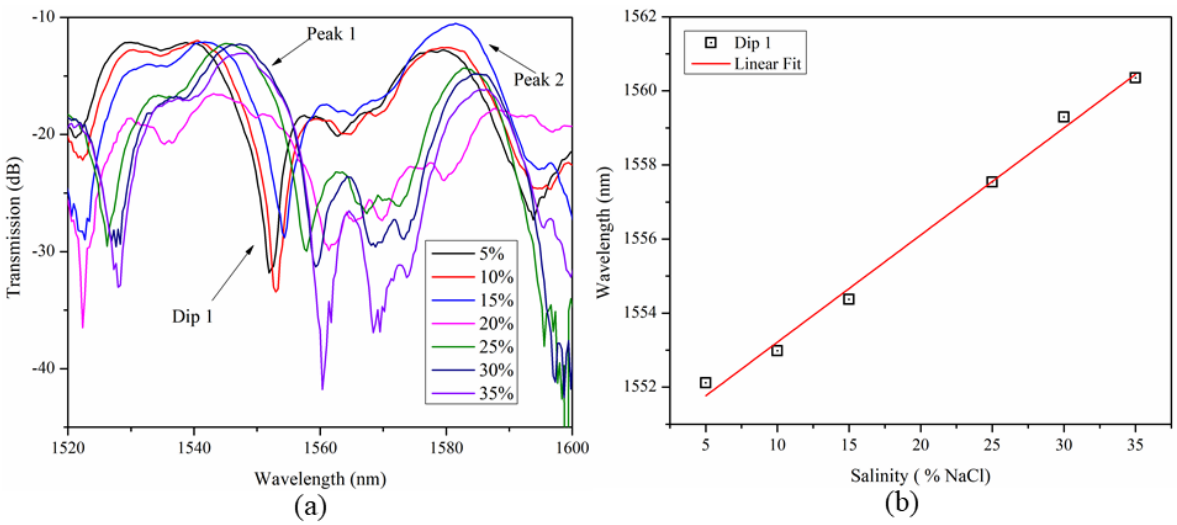


Figure 29 – (a) Transmitted spectrum for the change in salinity percentage for the SM1S sensor, (b) wavelength variation with salinity at Dip 1.

3.4.1.2 – SM2S

In this experiment, the SM2S structure uses the multimode fiber with 105/125 µm core/cladding diameters. Figure 30 (a) shows the transmitted spectrum of the sensor with the two peaks and two dips chosen to be measured. Figure 30 (b) depicts the best sensitivity at Dip 1. The sensitivity value is 34 pm/% of NaCl with R^2 equals to 0.986. The wavelength varies from 1593.6 nm to 1594.8 nm. Compared to the SM1S sensor, the SM2S presents a worse sensitivity since its MMF possesses a structure with a core and a cladding and also due to the splices losses which may be larger.

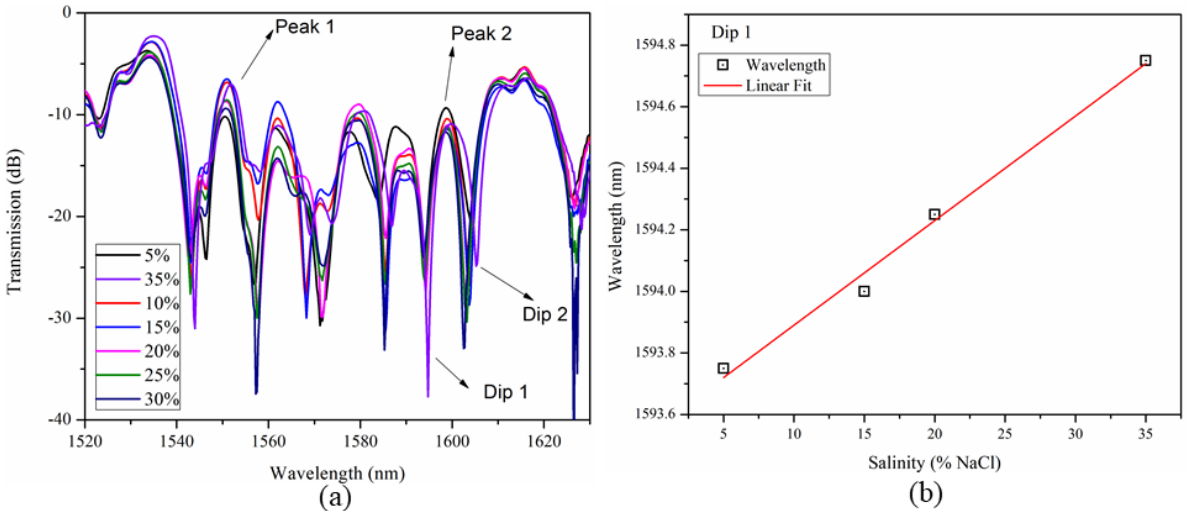


Figure 30 – (a) Transmitted spectrum for the change in salinity percentage for the SM2S sensor, (b) wavelength variation with salinity at Dip 1.

3.4.1.3 – SM1SM1S

The transmitted spectrum from the SM1SM1S sensor with one peak and three dips chosen to be measured is depicted in figure 31 (a). The SM1SM1S sensor uses the no core multimode fibers (125µm) as the MMFs. Figure 31 (b) presents Dip 3 nonlinear response with R^2 equal to 0.99, with a maximum sensitivity of 217.2 pm/%, a minimum sensitivity of 37.2 pm/% and an average sensitivity of 127.2 pm/%. For the range of 10

to 30% of NaCl in water the sensitivity is almost linear, with R^2 = 0.975, and a sensitivity value of 147 pm/%. Also comparing to the SM1S sensor, the SM1SM1S presents a worse sensitivity because there are two more splices between the fibers which increase the structure losses reducing the sensitivity. Also comparing to the SM1S the wave patterns are more confined due to the change in the structure that is, the addition of the SMF and one MMF of no core to the end of the SM1S which, changes its pattern.

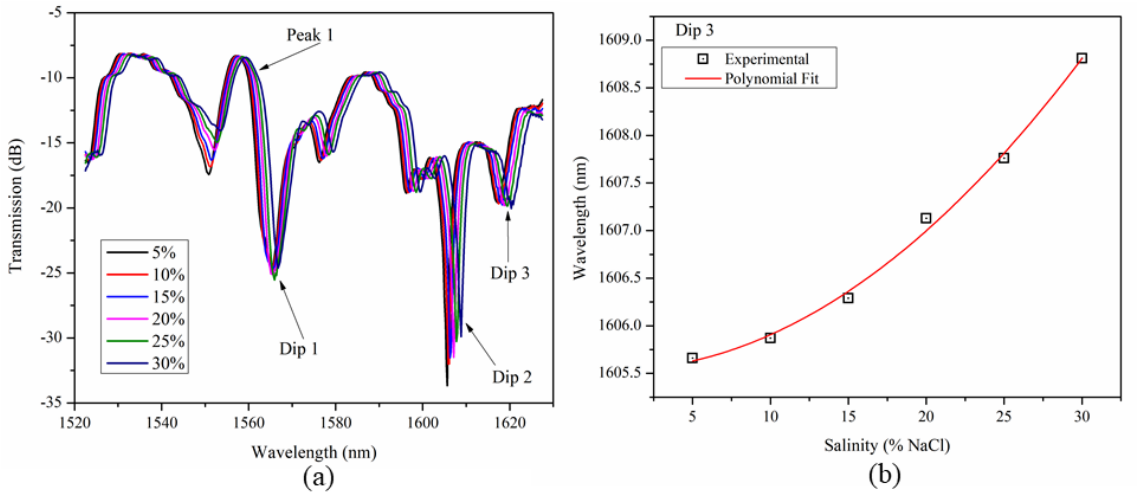


Figure 31 – (a) Transmitted spectrum for the change in salinity percentage for the SM1SM1S sensor, (b) wavelength variation with salinity at Dip 3.

3.4.1.4 – SM1SM2S

The transmission spectrum of the SM1SM2S sensor is shown in figure 32 (a) for different values in the percentage of saline solution. Sensitivity attained for the sensor at Dip 5 is shown in figure 32 (b). Dip 5 presents nonlinear response with R^2 = 0.987, with a maximum sensitivity of 402.6 pm/%, minimum sensitivity of 134.5 pm/% and average sensitivity of 268.5 pm/%. In this case, we believe that the SM1SM2S sensor presented a larger sensitivity because the refractive index of the MMF M2 cladding is smaller than that of the MMF M1 (therefore, closer to the salinity liquid refractive index).

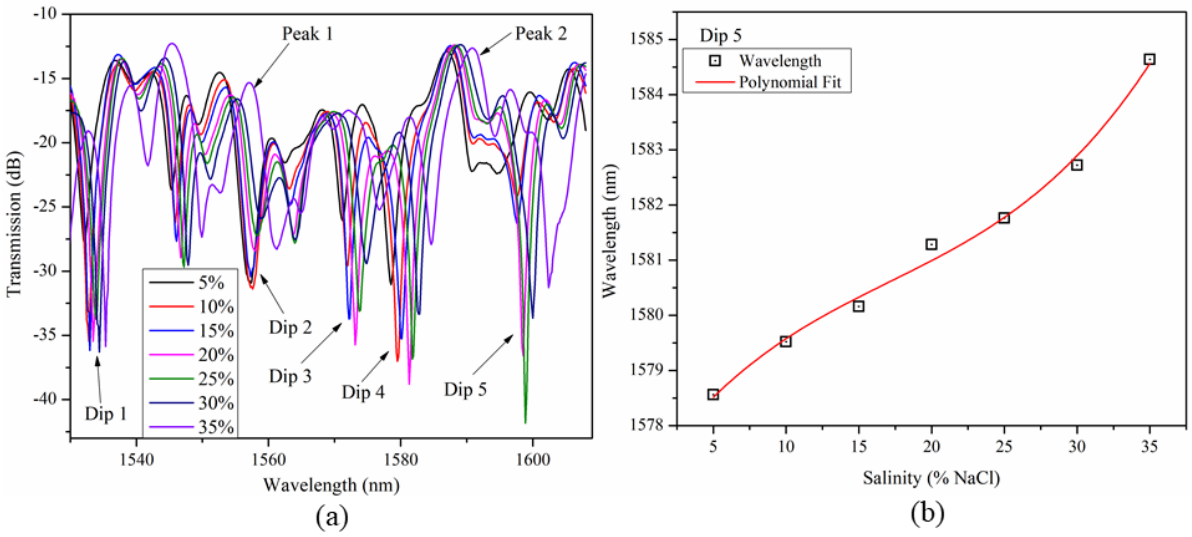


Figure 32 – (a) Transmitted spectrum for the change in salinity percentage for the SM1SM2S sensor, (b) wavelength variation with salinity at Dip 5.

3.4.1.5 – SM1M2S

Variation in the spectrum due to the change in the saline solution is shown in figure 33 (a) where many dips and peaks can be observed in the transmitted spectrum. Three dips and two peaks are chosen because of their good sensitivities. Dip 3 shows a good sensitivity with good linear response with R^2 equal to 0.98 and a sensitivity of 169.9 pm/% NaCl, as can be noted in figure 33 (b).

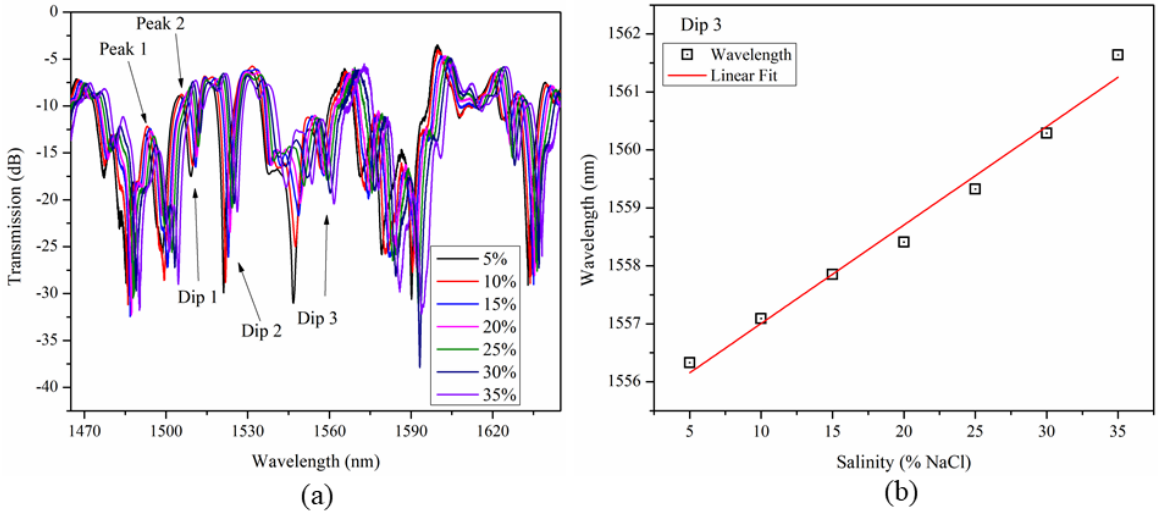


Figure 33 – (a) Transmitted spectrum for the change in salinity percentage for the SM1M2S sensor, (b) wavelength variation with salinity at Dip 3.

Table 3 shows the characteristics of the sensors for salinity measurement using the CDM structures. From Table 3, it can be concluded that the SM1SM2S sensor shows the best sensitivity among all the CDM structures with 402 pm/%. The SM1SM2S sensor presented the best sensitivity because the refractive index of M2 cladding is less than the refractive index of M1. The external medium influences the sensor the most because the smaller refractive index is closer to the salinity liquid refractive index. SM1S is the sensor which shows the second best sensitivity. The other structures are also adequate for the application because they are also showing good sensitivities except SM2S.

Table 3 – Characteristics of the sensors for salinity measurement for CDM sensor

Sensor	**Response**	**R^2**	**Maximum Sensitivity (pm/%)**
SM1S	Linear	0.99	289.3
SM2S	Linear	0.986	34.0
SM1SM1S	Nonlinear	0.99	217.2
SM1SM2S	Nonlinear	0.987	402.6
SM1M2S	Linear	0.98	169.9

3.4.2 – CDM structures with the balloon shaped structure

3.4.2.1 – SM1SM1S

Variation in the spectrum due to the change in the saline solution is shown in figure 34 (a) where three dips and two peaks can be chosen in the transmitted spectrum. Peak 2 shows a good sensitivity with good linear response to change in salinity percentage. R^2 is equal to 0.984 and a sensitivity of 168 pm/% NaCl was achieved. The wavelength as a function of salinity can be observed in figure 34 (b).

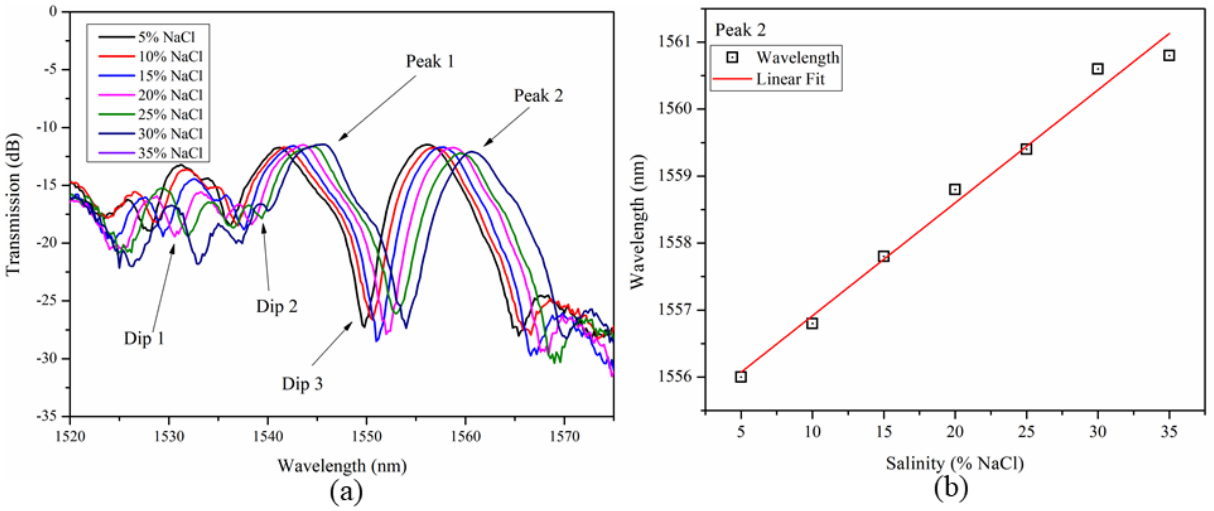


Figure 34 – (a) Transmitted spectrum for the change in salinity percentage for the combination of the SM1SM1S and balloon shaped sensor, (b) wavelength variation with salinity at Peak 2.

3.4.2.2 – SM1SM2S

The transmitted spectrum for the combined SM1SM2S and balloon shaped sensor is illustrated in figure 35 (a). Three peaks and one dip can be observed with good sensitivities in the transmitted spectrum which can be utilized to obtain the sensitivity of the sensor. Figure 35 (b) presents Peak 2 nonlinear response with R^2 equal to 0.987, with a maximum sensitivity of 109.1 pm/%, a minimum sensitivity of 19.1 pm/% and an

average sensitivity of 64 pm/%. For the range from10 to 30% of NaCl in water the sensitivity is almost linear, $R^2 = 0.972$, with a sensitivity value of 96 pm/%.

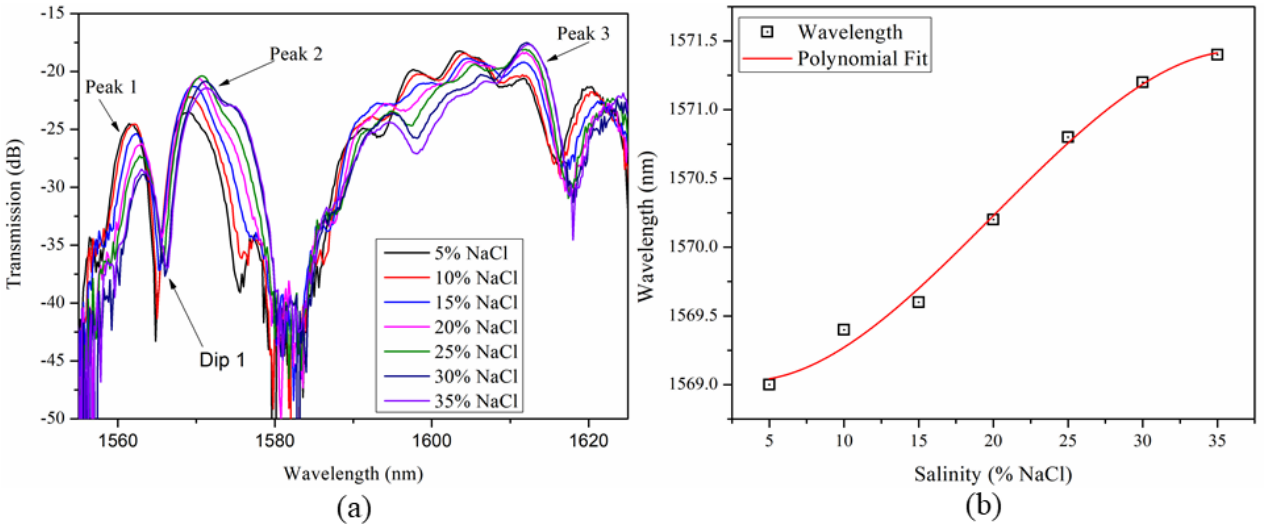


Figure 35 – (a) Transmitted spectrum for the change in salinity percentage for the combination of the SM1SM2S and balloon shaped sensor, (b) wavelength variation with salinity at Peak 2.

3.4.2.3 – SM1M2S

Figure 36 (a) presents the transmission spectrum of the SM1M2S and Balloon shaped sensor for different values in the percentage of saline solution. Sensitivity attained for the sensor at Peak 1 is shown in figure 36 (b). Peak 1 presents high linear response with $R^2 = 0.9936$ and the sensitivity of the sensor is 113.5 pm/%.

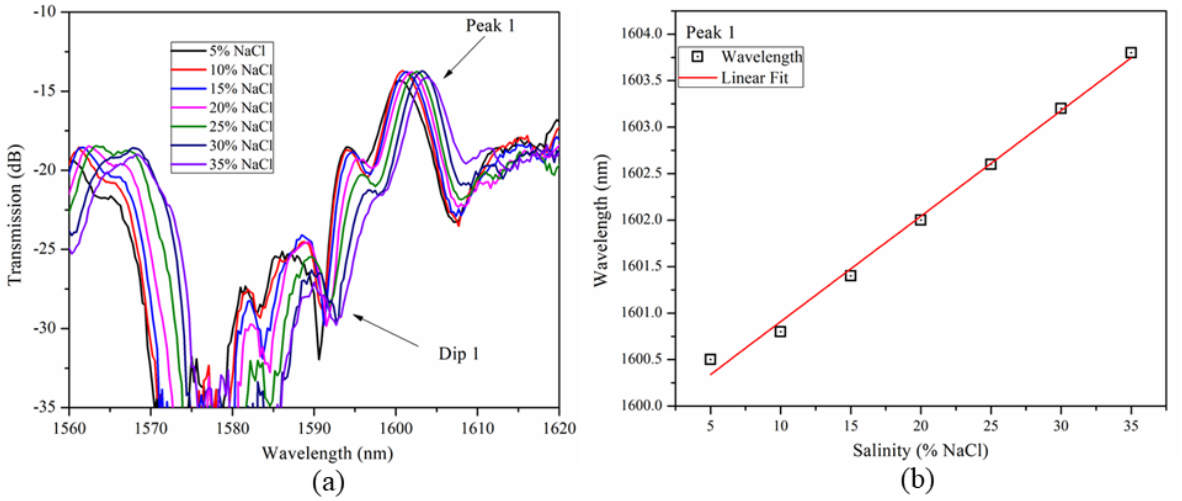


Figure 36 – (a) Transmitted spectrum of the combined SM1M2S and balloon shaped sensor for salinity, (b) wavelength variation at Peak 1.

Table 4 summarizes the sensitivities and responses of the sensors for salinity measurement for the combination of CDM structures and balloon shaped sensor. The SM1SM1S sensor shows the best sensitivity among all the three structures with a value of 168 pm/%. Its multimode fibers are both no core fibers which are in direct contact with the external refractive index and therefore are more intensely affected by refractive index variations, i. e., salinity changes, leading to an increase in the sensitivity. Among the sensors, the SM1SM1S sensor exhibits a better sensitivity of 35% and 32% than the SM1SM2S and SM1M2S sensors, respectively.

Table 4– Characteristics of the sensors for salinity measurement for CDM and balloon shaped sensor.

Sensor	**Response**	**R^2**	**Maximum Sensitivity (pm/%)**
SM1SM1S	Linear	0.984	168.0
SM1SM2S	Nonlinear	0.987	109.1
SM1M2S	Linear	0.9936	113.5

Comparison to previous published results in the literature can be observed in Table 5, where the sensitivity and the complexity of the sensors structures are described. The characteristic of straightforward fabrication procedure and low cost turns the proposed sensor very promising and attractive in several applications.

Table 5 – Comparison to some literature sensors for salinity measurement

Configuration	Sensitivity (pm/%)	Structure	References
Microfiber MZ interferometer	208	Complex	51
Fiber Fabry–Perot interferometer	95.5	Simple	75
Microfiber Sagnac Interferometer	1950	Complex	76
C-type fiber structure	1402	Complex	77
SM1SM1S and balloon shaped	168	Simple	This work

However, it is important to mention that, in the case of the salinity measurement, the inclusion of the balloon shaped structure does not improve the sensibility of the sensors. Salinity measurements for the CDM structure show good sensitivity as compared to the combination of the balloon and the CDM structure, where it can be said that the balloon sensor is not a good sensor for the salinity because of the salinity liquid lower refractive index, in the 1.338 range.

3.5 – Results for Temperature Measurement

3.5.1 – CDM structures Only

3.5.1.1 – SM1S

The experiments were performed in the range from 23.8 °C to 71.4 °C. Figure 37 (a) illustrates the variation in the spectrum for the change in temperature. Figure 37 (b) shows the nonlinear response for the Dip 2. The maximum sensitivity is 135.9 pm/°C, minimum sensitivity is 41.05 pm/°C and average sensitivity is 88.47 pm/°C for the SM1S temperature sensor with R^2 equals to 0.987.

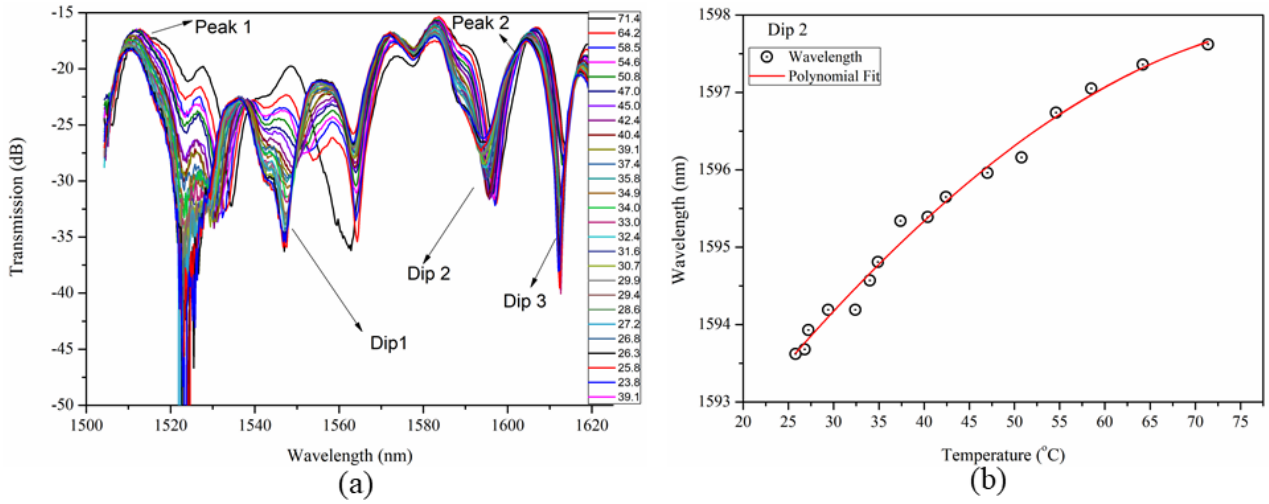


Figure 37 – (a) Transmitted SM1S Sensor spectrum variation with change in temperature, (b) wavelength as a function of the temperature for Dip 2.

3.5.1.2 – SM2S

The hot water temperature, in this case, varies from 23.5°C to 70.1°C as can be observed in Figure 38 (a) for this sensor. Three Peaks and three Dips can be utilized to calculate the sensitivity of the SM2S sensor. Dip 2 varies in the range of 1582 nm to 1596 nm with the change in the temperature. Figure 38 (b) shows the best sensitivity, attained at Dip 2, with a value of 233.30 pm/°C and R^2 = 0.989 for the SM2S sensor. We believe that the larger sensitivity obtained in this case, compared to the SM1S sensor, is due to the lower refractive index of the cladding of the MMF M2 fiber.

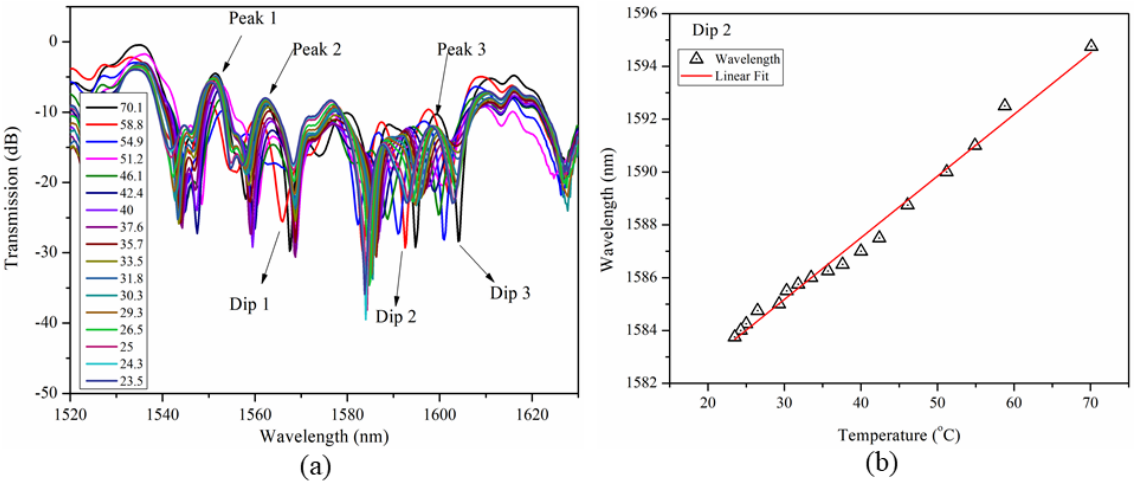


Figure 38 – (a) Transmitted SM2S Sensor spectrum variation with change in temperature, (b) wavelength as a function of the temperature for Dip 2.

3.5.1.3 – SM1SM1S

The temperature variation, in this case, was from 23.5°C to 54°C. In Figure 39 (a) the change in the spectrum due to the temperature is depicted. Peak1, Dip 1 and Dip 2 are being selected to calculate the sensitivity of the temperature sensor. Peak 1 varies in the range of 1544 nm to 1559 nm where Dip 1 changes in the range of 1535 nm to 1550 nm and Dip 2 deviates in the range of 1545 nm to 1560 nm. The best sensitivity was achieved for the Dip 1 with maximum sensitivity of 377.62 pm/°C, minimum sensitivity of 17.09 pm/°C and an average sensitivity of 197.35 pm/°C. Figure 39 (b) shows the nonlinear response of the sensor with R^2 equal to 0.982. In this case, the two MMFs were no core fibers and therefore, they permit the evanescent field to be in direct contact with the hot water, increasing the sensor sensitivity.

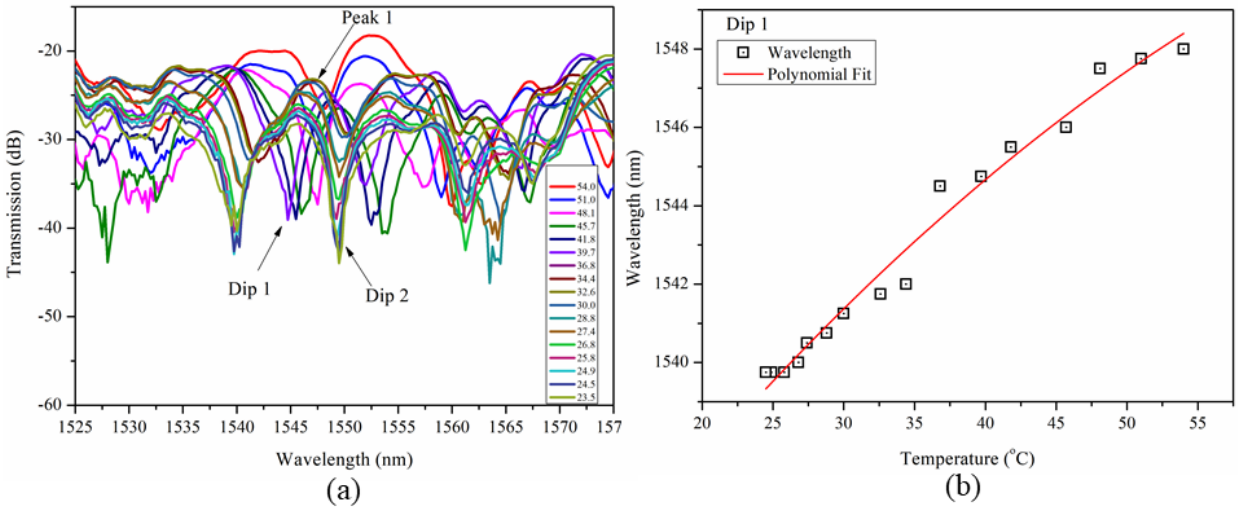


Figure 39 – (a) Transmitted SM1SM1S Sensor spectrum variation with change in temperature, (b) wavelength as a function of the temperature for Dip 1.

3.5.1.4 – SM1M2S

In this case, the temperature was varied from 22.8°C to 69.7°C. The spectrum change due to the temperature is presented in Figure 40(a). The best sensitivity is obtained at Dip 1 with a value of 180.52 pm/°C and R^2 equals to 0.993 in the temperature range of 22.8°C to 40°C. The sensor linear behavior is shown in Figure 40(b). The use of one MMF fiber (M1) else, when compared to the SM2S sensor, increased the splices losses leading to a smaller sensitivity.

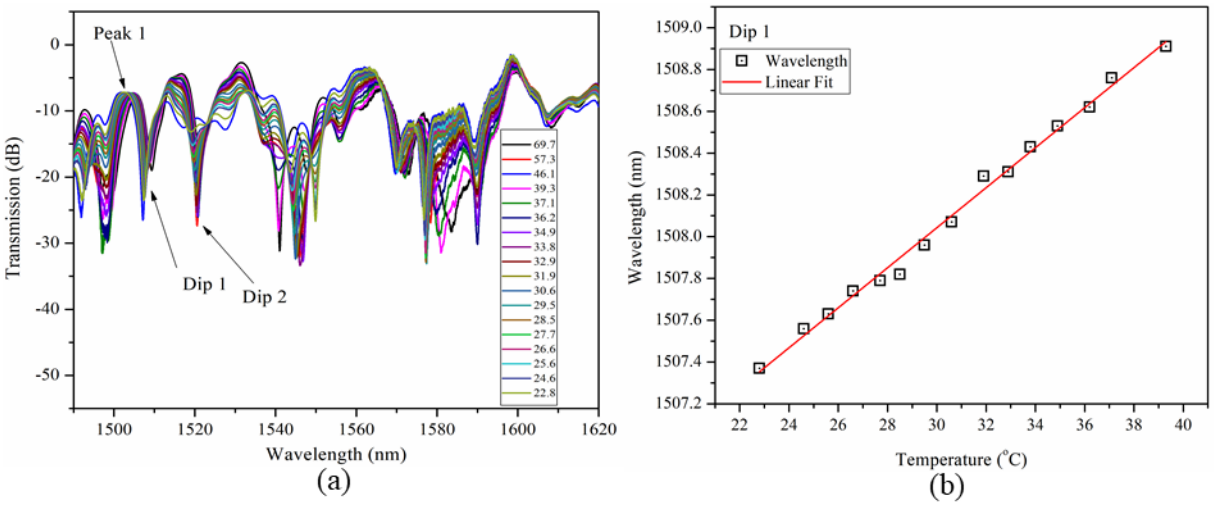


Figure 40 – (a) Transmitted SM1M2S Sensor spectrum variation with change in temperature, (b) wavelength as a function of the temperature for Dip 1.

3.5.1.5 – SM1SM2S

Variation in temperature from 20.2°C to 64°C is shown in Figure 41 (a) with several peaks and dips. From figure 41 (b), it can be noted that Dip 2 presents a linear response with a sensitivity equal to 170.59 pm/°C and R^2 equal to 0.979. Since only one of the MMFs is a no core fiber in this case, the sensitivity is worse when compared to the SM1SM1S sensor.

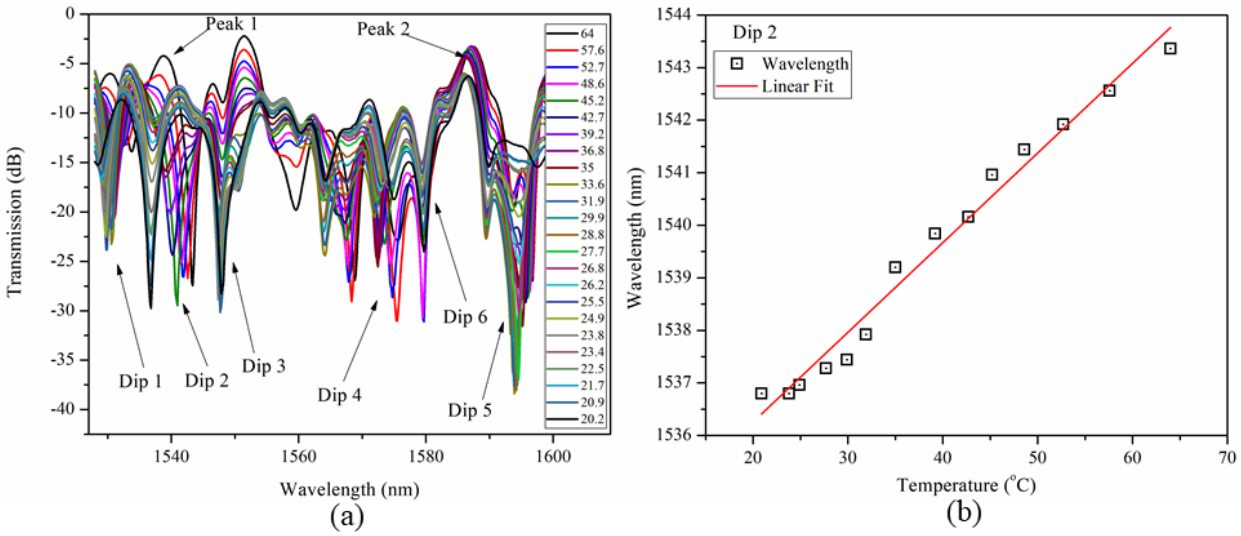


Figure 41 – (a) Transmitted SM1SM2S Sensor spectrum variation with change in temperature, (b) wavelength as a function of the temperature for Dip 2.

Table 6 shows the characteristics for temperature measurement for all the CDM sensors. It is noted that SM1SM1S shows the best sensitivity among all the CDM structures with a maximum value of 377.62 pm/°C. Since the temperature measurement was developed in a watery environment, again the no core fibers were fundamental for this result, as they enable the evanescent field to be in direct contact to the hot water.

Table 6 – Characteristics of the sensors for temperature measurement for CDM sensors only

Sensor	**Response**	**R^2**	**Maximum Sensitivity (pm/°C)**
SM1S	Nonlinear	0.987	135.90
SM2S	Linear	0.989	233.30
SM1SM1S	Nonlinear	0.982	377.62
SM1SM2S	Linear	0.979	170.59
SM1M2S	Linear	0.993	180.52

3.5.2 – CDM structures with the balloon shaped structure

3.5.2.1 – SM1SM1S

Variation in the sensor spectrum due to the change in temperature from 21.1°C to 41 °C is shown in figure 42 (a). Since the variation of the wavelength with temperature was difficult to obtain in this case, it was decided to analyse the transmission loss change due to temperature variation. As the temperature rises from 21.1°C to 41°C, the transmission loss is decreased as depicted in figure 42 (b). A linear response for the sensor is achieved at Peak 3 with $R^2 = 0.989$ and the sensitivity value is 0.189 dB/°C in the temperature range of 22.8°C to 32.7°C.

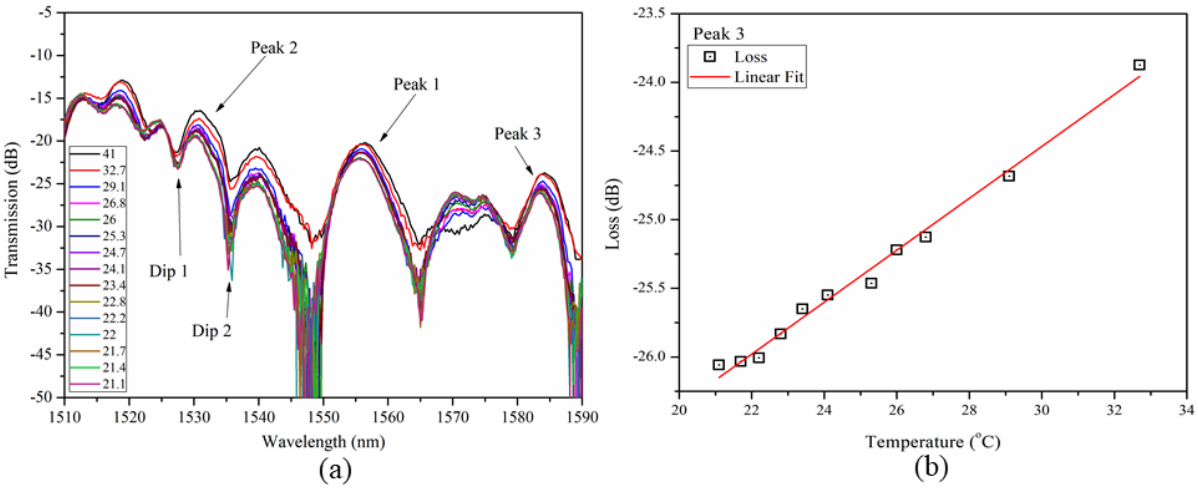


Figure 42 – (a) Transmitted spectrum of the combined SM1SM1S and balloon shaped sensor for temperature variation, (b) loss variation with temperature for Peak 3

3.5.2.2 – SM1SM2S

The sensor transmitted spectrum variation is depicted in figure 43 (a). Few peaks and dips can be used to obtain the sensitivity of the sensor. Figure 43 (b) shows a nonlinear response for Peak 1 with $R^2 = 0.99$ and a maximum sensitivity value of 1.432 dB/°C. The minimum sensitivity value is 0.774 dB/°C. The average sensitivity is 1.103 dB/°C. Also, in this case, the transmission loss was evaluated. The sensitivity is larger than the SM1SM1S sensor because the splicer losses are smaller.

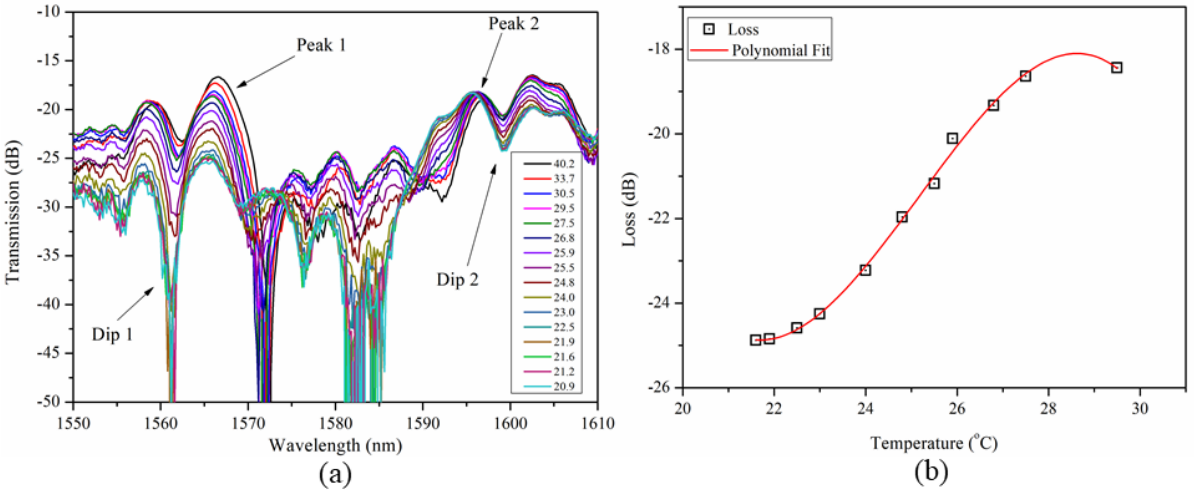


Figure 43 – (a) Transmitted spectrum of the combined SM1SM2S and balloon shaped sensor for temperature variation, (b) loss variation with temperature for Peak 1.

3.5.2.3 – SM1M2S

Figure 44 (a) shows the variation in the spectrum due to the variation in temperature. As the temperature increased, Dip1 moved towards a longer wavelength. Dip 1 exhibits a nonlinear response, as shown in figure 44 (b), with $R^2 = 0.987$ and a maximum sensitivity of 735.6 pm/°C, a minimum sensitivity of 126.1 pm/°C and an average sensitivity of 430.85 nm/°C.

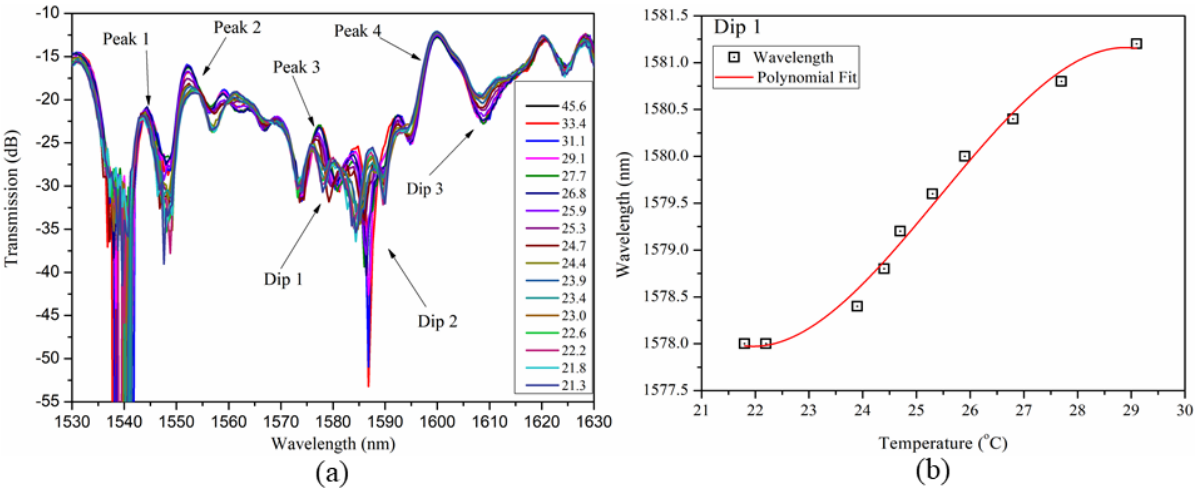


Figure 44 – (a) Transmitted spectrum of the combined SM1M2S and balloon shaped

sensor for temperature variation, (b) wavelength variation with temperature for Dip 1.

Table 7 summarizes the sensors characteristics for temperature measurement for the combination of the balloon shaped structure and CDM structures. The SM1M2S structure combined to the balloon structure shows a good sensitivity with a maximum value of 735.6 pm/°C. The SM1M2S structure does not have a singlemode fiber in the middle of the two multimode fibers, this improves its sensitivity because the singlemode fiber is much less influenced by temperature changes than multimode fibers, especially when compared to no core fibers, in watery environment. It is important to mention that, in this case, the balloon shaped structure was fundamental to the improvement in the SM1M2S sensitivity since when compared to the SM1M2S sensor only, the increase in the sensitivity was around 300%.

Table 7 – Characteristics of the sensors for temperature measurement for CDM and balloon shaped sensor.

Sensor	**Response**	**R^2**	**Maximum Sensitivity**
SM1SM1S	Linear	0.989	0.189 dB/°C
SM1SM2S	Nonlinear	0.990	1.432 dB/°C
SM1M2S	Nonlinear	0.987	735.6 pm/°C

Most of the researchers reports the temperature sensitivity in terms of wavelength shift per degree centigrade and very few determined the sensitivity based on the power loss per degree centigrade. Hence, the SM1M2S and balloon shaped sensor is compared to previous experimental results published in the literature as presented in Table 8. It can be concluded that the SM1M2S structure combined to the balloon structure shows the best sensitivity among all the structures exhibited in Table 8. The proposed SM1M2S and balloon shaped structures can, then, be a great combination for temperature measurement in many applications as it shows a good sensitivity compared to other sensors.

Table 8 – Comparison to some previous results published in the literature for temperature measurement

Configuration	Sensitivity	References
Macro bent fiber Bragg grating	31.7 pm/°C	78
Two semi-circular bending	260 pm/°C	79
Bent-SMF with LPG	42.9 pm/°C	80
Balloon bent fiber	22.9 pm/°C	81
SM1M2S and balloon shaped sensor	735.6 pm/°C	This work

3.6 – Results for Simultaneous Temperature and Salinity Measurements

For the simultaneous salinity and temperature measurements, the combined SM1SM2S and balloon shaped structures sensor was chosen to be presented here since it showed the best results when compared to the SM1SM1S and SM1M2S with the balloon shaped structure sensors.

Variation in the temperature was applied to the SM1SM2S structure while salinity variation was applied to the balloon shaped structure at the same time. The measurements were carried out for NaCl liquids with concentration from 10 to 25% with an interval of 5% and the temperature range was changed from 21 to 42 °C. The dip around 1600 nm was analyzed for all values of salinity and temperature. Figures 45 (a), 46 (a), 47 (a) and 48 (a) show the variation in the transmitted spectrum for simultaneous measurement of temperature and salinity at 10%, 15%, 20% and 25% of NaCl saline solutions, respectively. Figures 45 (b), 46 (b), 47 (b) and 48 (b) illustrate the power loss variation with respect to the temperature and present good sensitivities. In these cases, the wavelength variation was also difficult to attain. Therefore, the transmission loss was evaluated, as well.

Table 9 summarizes the sensitivity and response of the SM1SM2S with the balloon shaped sensor for simultaneous measurement with respect to the different NaCl

saline solution. It was found that the SM1SM2S with the balloon shaped sensor presents a nonlinear response with a maximum sensitivity of 2.86 dB/°C at 10% NaCl saline solution. The sensor demonstrated a good sensitivity to temperature in all range of saline solutions. Although the CDM structure, SM1SM2S, presents a singlemode fiber between the two multimode fibers, which may cause a decrease in the sensitivity to temperature, the balloon shaped structure was immersed in the saline solution, and it helped to improve the sensor's sensitivity. The results demonstrate that the proposed sensor can be utilized to measure two parameters, temperature and salinity, simultaneously.

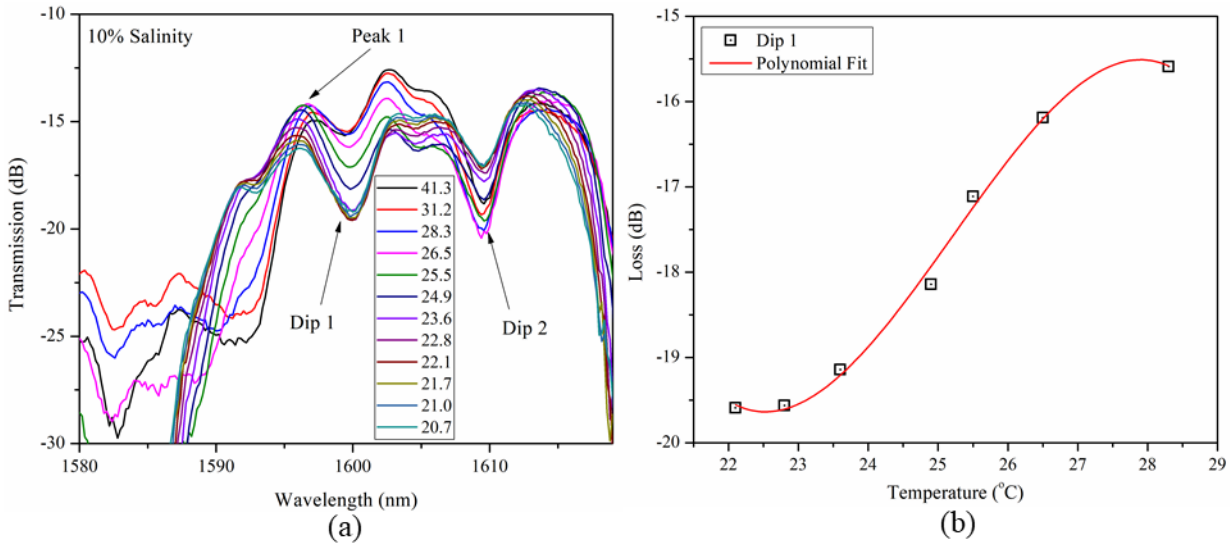


Figure 45 – (a) Variation in the SM1SM2S and balloon shaped sensor transmitted spectrum for simultaneous measurement at 10% of saline solution, (b) response at Dip 1.

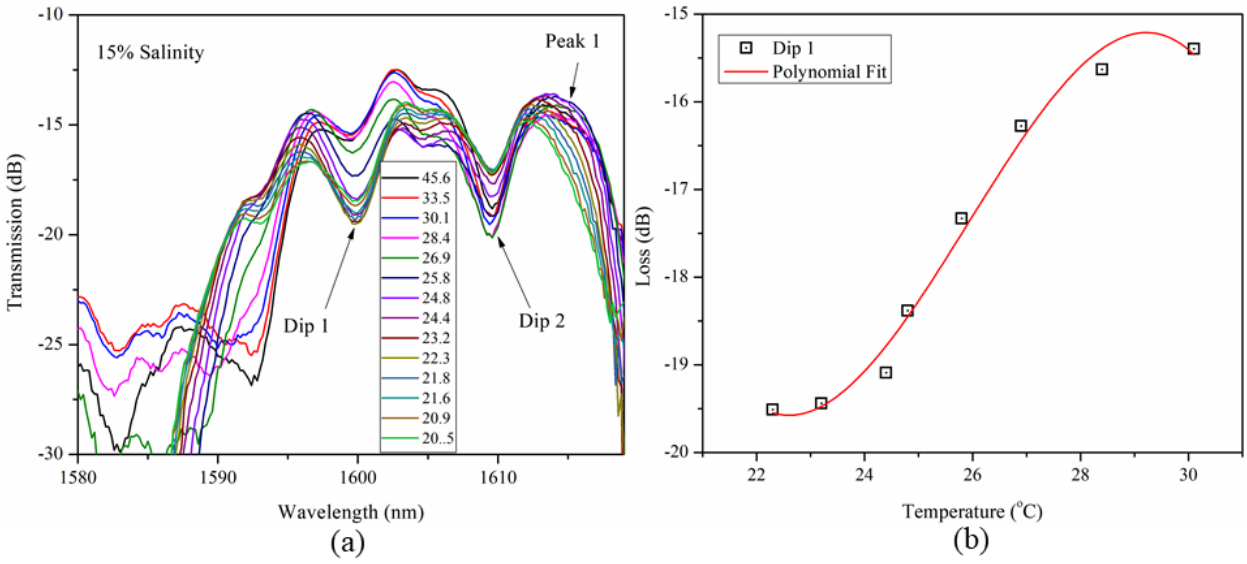


Figure 46 – (a) Variation in the SM1SM2S and balloon shaped sensor transmitted spectrum for simultaneous measurement at 15% of saline solution, (b) response at Dip 1

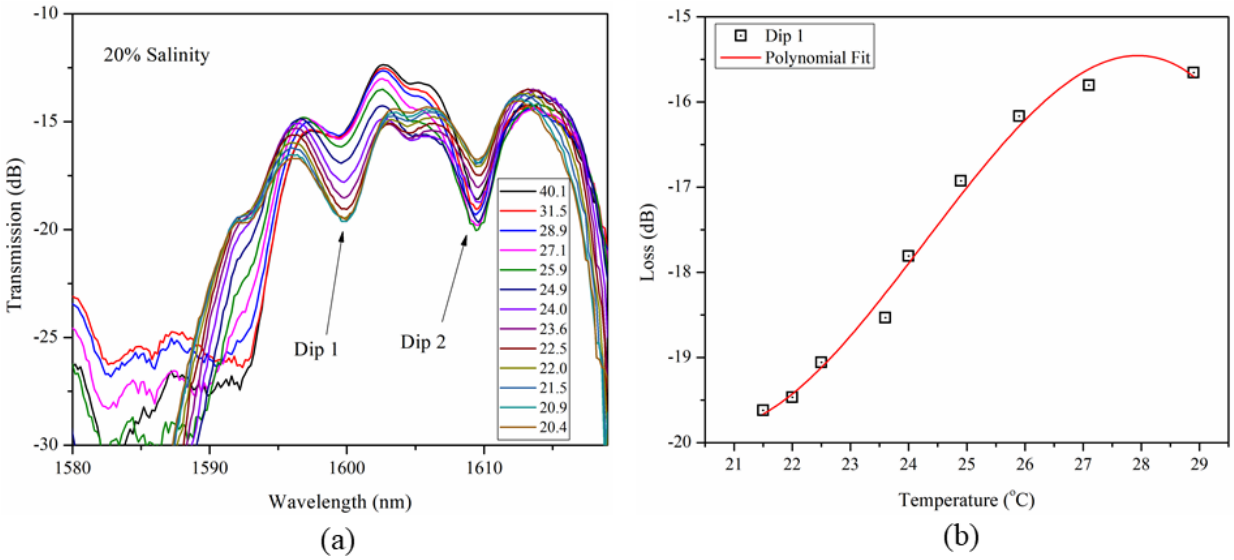


Figure 47 – (a) Variation in the SM1SM2S and balloon shaped sensor transmitted spectrum for simultaneous measurement at 20% of saline solution, (b) response at Dip 1

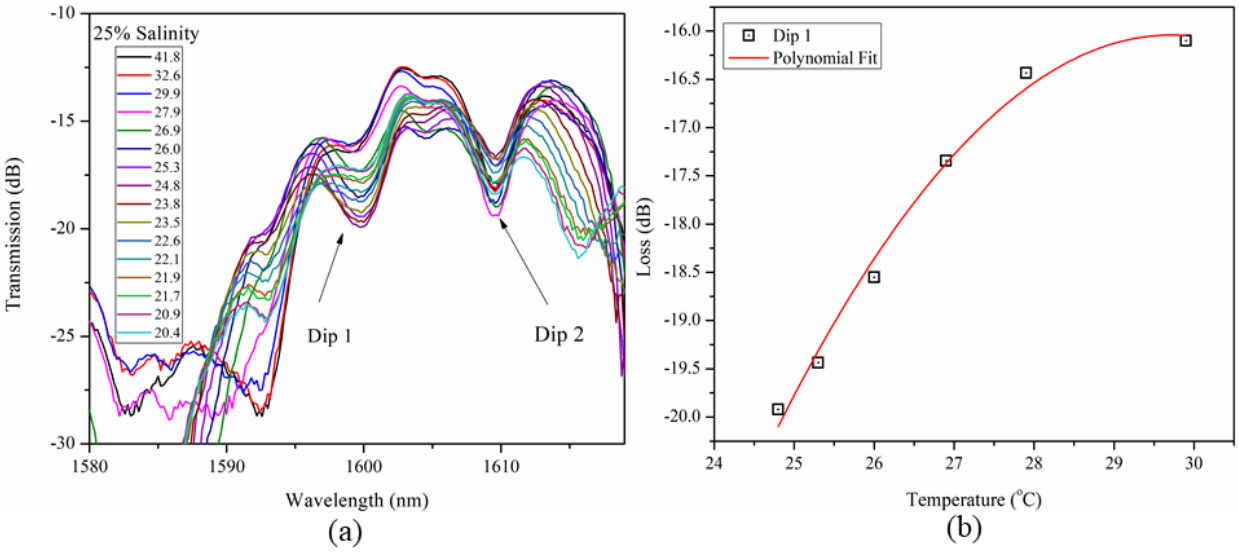


Figure 48 – (a) Variation in the SM1SM2S and balloon shaped sensor transmitted spectrum for simultaneous measurement at 25% of saline solution, (b) response at Dip 1.

Table 9 – Characteristics of the SM1SM2S and balloon shaped sensor for simultaneous measurement of temperature and salinity

Salinity %	**Response**	**R^2**	**Maximum sensitivity (dB/°C)**
10	Nonlinear	0.991	2.86
15	Nonlinear	0.981	1.22
20	Nonlinear	0.986	1.37
25	Nonlinear	0.985	1.65

It is important to mention that for the salinity only, the balloon shaped structure (together with the CDM structures) does not help to improve the sensitivity of the sensors since the sensitivities were always lower in these measurements. However, for the simultaneous measurement, the balloon shaped structure together with the SM1SM2S structure presented a higher sensitivity as compared to the case of the temperature measurement. It occurs because, in the temperature measurement, the

balloon shaped structure was immersed in distilled water (n = 1.33), while in the simultaneous measurement, the balloon shaped structure was immersed in the salinity liquid, whose refractive indexes were greater than 1.341. Therefore, the influence of the external refractive index on the sensor is more intense, in this case.

3.7 – Simulation Results using the BPM software

In this section the results concerning the simulations developed using the BPM software are presented. All the simulation results will be compared to the experimental ones and therefore, they will be shown together. CDM sensors only are presented. Due to the Covid Pandemic situation, it was impossible to perform the balloon shaped structure simulation.

3.7.1 – Results for Salinity Simulation

3.7.1.1 – SM1S

In this case, the salinity sensor is formed by the SM1S structure. The simulation and experimental results are compared and presented in Figure 49. It can be observed that the experimental and simulation results follow the same trend. The difference between these results can be explained due to the different simulation and experimental environments.

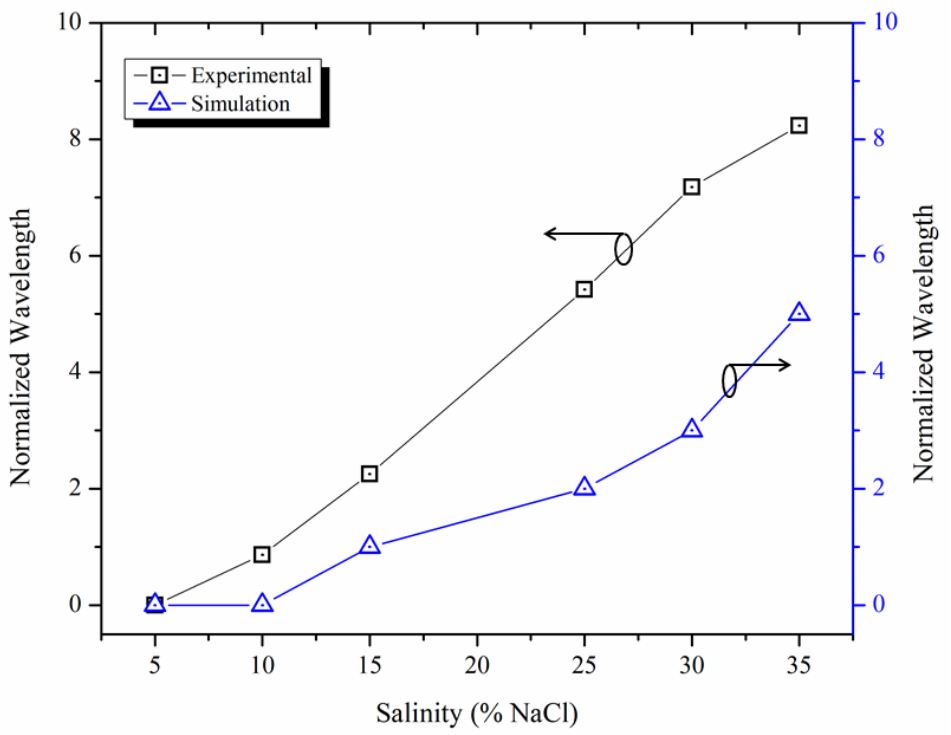


Figure 49 – Comparison of experiment and simulation results for the SM1S structure as a salinity sensor.

3.7.1.2 – SM2S

Comparisons of simulated and experimental results are illustrated in figure 50 for the SM2S salinity sensor. Experimental and simulation results present a large wavelength difference. Wavelength difference may be due to the fabrication process of the CDM structure which may be not accurate and for the experimental results, the MMF M2 does not operate at the reimaging point.

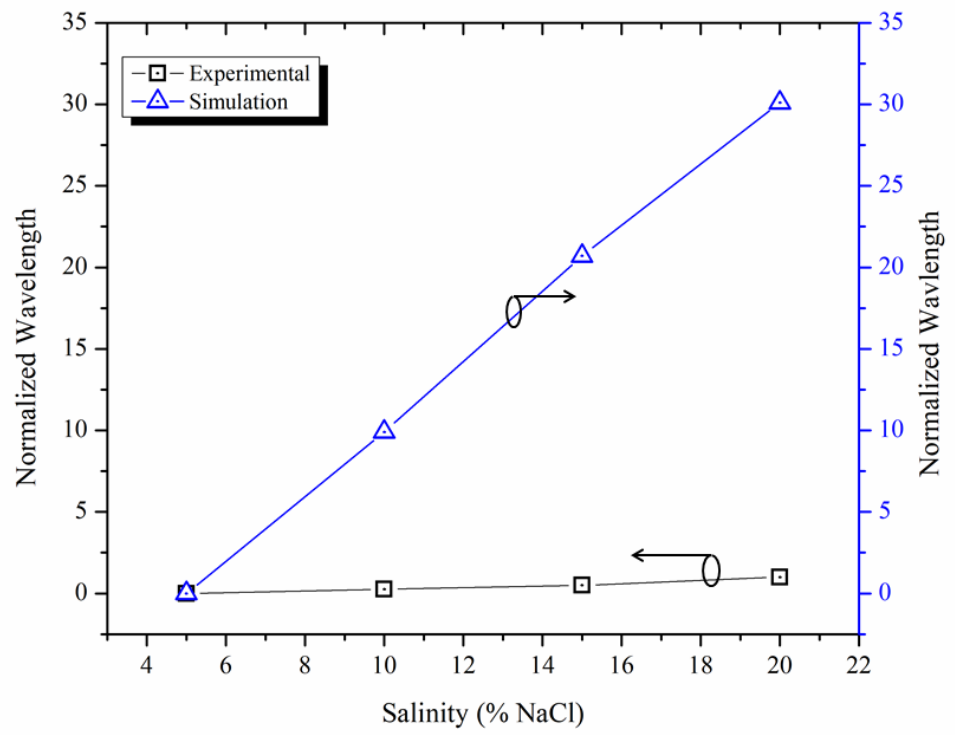


Figure 50 – Comparison of experiment and simulation results for the SM2S structure as a salinity sensor.

3.7.1.3 – SM1SM1S

Figure 51 shows experimental and numerical results for the SM1SM1S salinity sensor. Both curves follow the same pattern with a good agreement between the wavelengths.

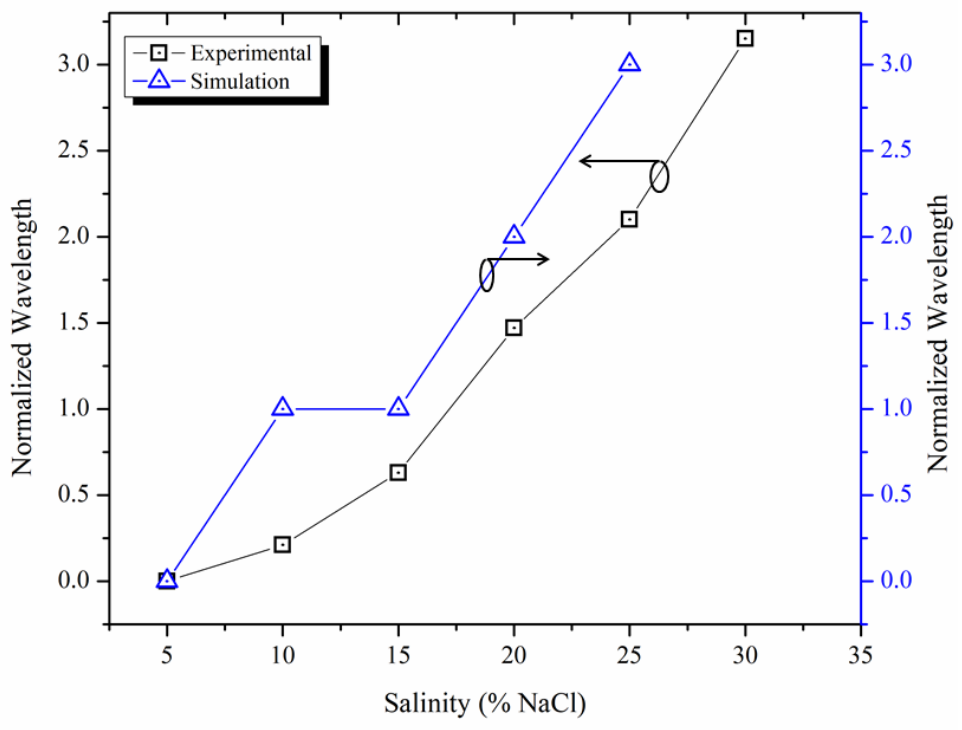


Figure 51 – Comparison of experiment and simulation results for the SM1SM1S structure as a salinity sensor.

3.7.1.4 – SM1M2S

The simulation and experimental results are compared in figure 52 for the SM1M2S salinity sensor. It is noted that the experimental and simulation results follow the same pattern with a difference in the wavelength. Again, the experimental fabrication process may be the cause of such difference together with the MMF M2 fiber which does not utilize the reimaging point.

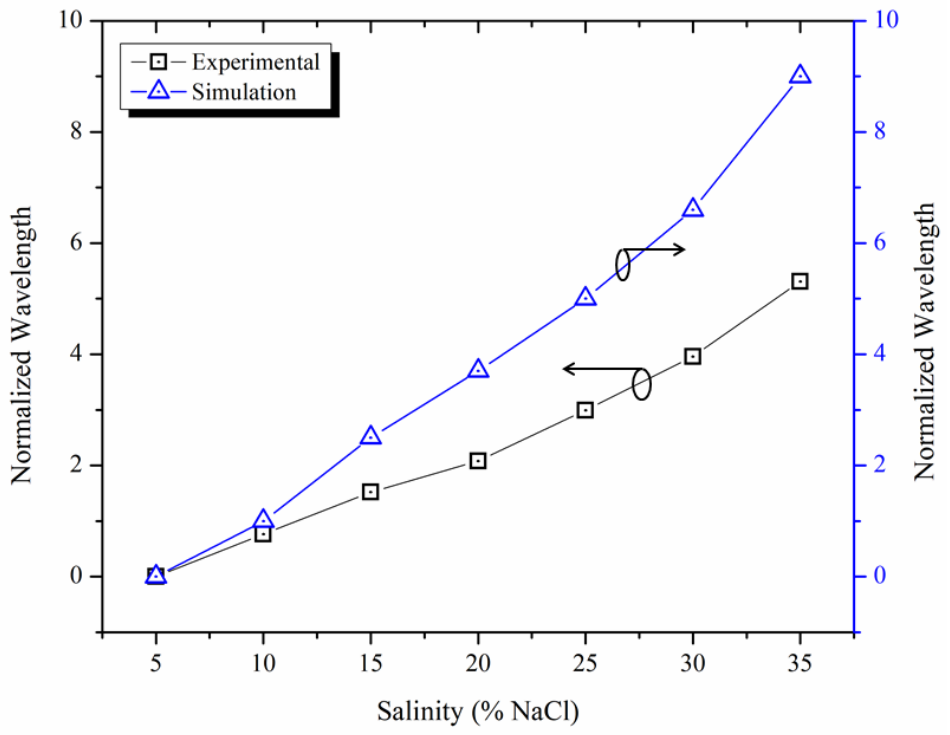


Figure 52 – Comparison of experiment and simulation results for the SM1M2S structure as a salinity sensor.

3.7.1.5 – SM1SM2S

Comparison between the simulated and experimental results for the SM1SM2S salinity sensor is depicted in Figure 53. The simulated results predicted the experimental results satisfactorily.

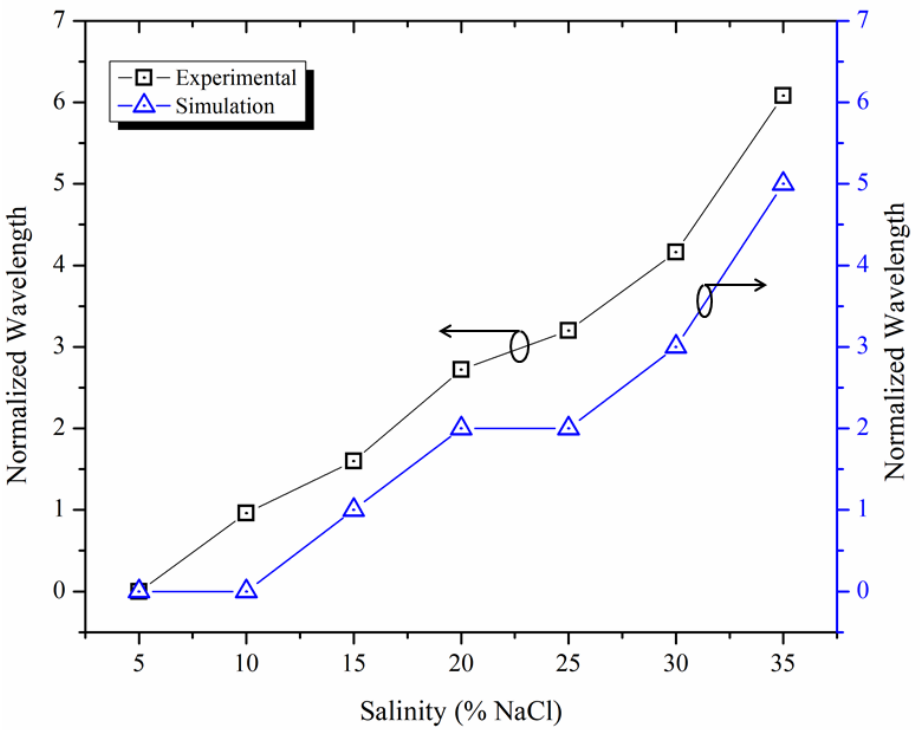


Figure 53 – Comparison of experiment and simulation results for the SM1SM2S structure as a salinity sensor.

3.7.2 – Results for Temperature Simulation

3.7.2.1 – SM2S

The simulation and experimental results are compared in Figure 54 for the SM2S temperature sensor and they follow the same trend but with a large difference in the wavelength. It is due to the fabrication of the sensor, the MMF M2 fiber which does not use the reimaging point and due to the difference in the simulation and experimental environments.

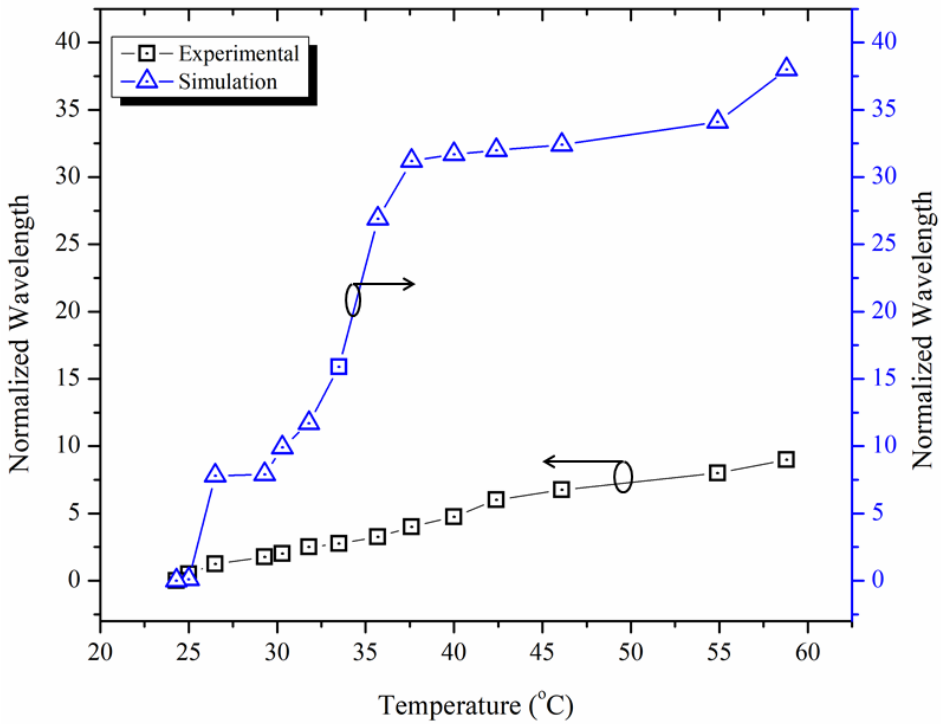


Figure 54 – Comparison of experiment and simulation results for the SM2S structure as a temperature sensor.

3.7.2.2 – SM1SM1S

Figure 55 presents the comparison of the simulated and experimental results for the SM1SM1S temperature sensor. The results show the same pattern but they do have a large wavelength difference. Wavelength difference may be due to the fabrication process and the difference in the simulation and experimental environments, as well.

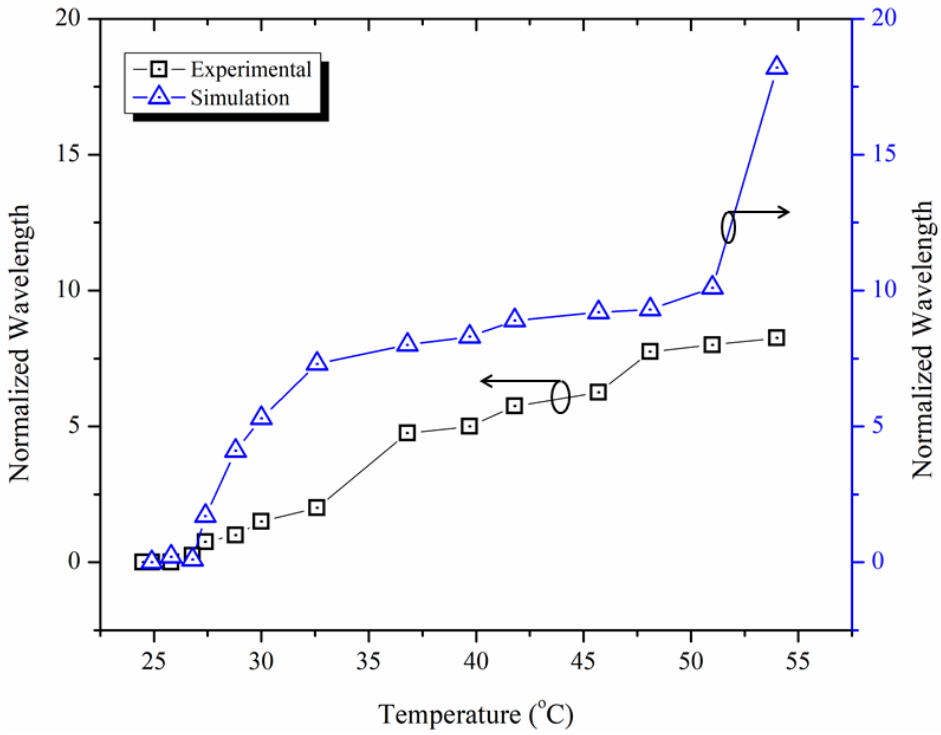


Figure 55 – Comparison of experiment and simulation results for the SM1SM1S structure as a temperature sensor.

4 – Conclusion and Perspective

In this work, salinity and temperature sensors were proposed. The devices researched (CDM and Balloon sensor) are all-fiber structures and present the advantage of being simple, easy to manufacture and inexpensive.

Fiber sensors based on different CDM structures measurement of salinity and temperature were presented. Salinity percentage in watery environment and temperature can be obtained from wavelength shift or optical power loss. For salinity measurement, SM1SM2S sensor shows the best sensitivity among all the CDM structures with 402 pm/%. The SM1SM2S sensor presented the best sensitivity because the refractive index of the MMF M2 cladding is smaller than that of the MMF M1, therefore, closer to the salinity liquid refractive index being much influenced by it.

For the temperature measurements, SM1SM1S shows the best sensitivity among all the structures with a maximum value of 377.62 pm/°C. Since the temperature measurement was developed in a watery environment, the no core fibers were fundamental for this result, as they were in direct contact to the hot water.

All-fiber sensors based on the combination of a SMF balloon shaped structure with different CDM structures were also used for the measurement of salinity and temperature. For salinity measurements, the SM1SM1S and balloon shaped sensor shows the best sensitivity among all the other structures with a value of 168 pm/% NaCl. Its multimode fibers are both no core fibers which are in direct contact with the external refractive index leading to an increase in the sensitivity. However, the obtained sensitivity is worse than that using only the CDM structure. Therefore, for a salinity measurement it is better to use the CDM structure alone, i. e., do not use the balloon together with the CDM structure.

For the temperature measurements, the SM1M2S structure combined to the balloon structure shows a great sensitivity with a maximum value of 735.6 pm/°C. The SM1M2S structure does not have a singlemode fiber in the middle of the two multimode fibers; this improves its sensitivity because the singlemode fiber is much less influenced by temperature changes than multimode fibers, especially compared to no core fibers, in watery environment.

Simultaneous salinity and temperature measurements were also performed. In this case, the response of the SM1SM2S with the balloon shaped sensor for simultaneous measurement with respect to the different NaCl saline solutions shows a maximum sensitivity of 2.86 dB/°C at 10% NaCl saline solution. The sensor showed a good sensitivity to temperature in all range of saline solutions. Although the CDM structure, the SM1SM2S, presents a singlemode fiber between the two multimode fibers, which may cause a decrease in the sensitivity to temperature, the balloon shaped structure was immersed in the saline solution, which helped the sensor to improve its sensitivity.

Sensors' simulations were accomplished for the CDM structures, as well. Due to the Covid Pandemic situation, it was impossible to perform the balloon shaped simulations.

Salinity simulations show the best result for the SM1SM2S sensor. The experiment and the simulation results confirm the same appearance with a small difference in wavelength. Beyond the fabrication process that is not accurate, the MMF M2 fiber was not cut at its reimaging point, all that leads to the difference between the experimental and simulation results.

Temperature simulations present the best result for the SM1SM1S sensor. The results show the same appearance but they do have a large wavelength difference. Wavelength difference may be due to the sensor fabrication process together with the difference in the experimental and simulation environments.

The results obtained in this work confirm the ability of the proposed sensors to measure temperature, salinity and the simultaneously measurement of these two parameters for environmental application.

4.1 – Suggestions for Future Works

The following are some suggestions for continuing this research:
The CDM sensors are needed to be further studied with different combinations of fibers.

The Balloon shaped structure as a salinity sensor and as a temperature sensor should be

implemented.

The simultaneous measurement should be executed varying the salinity applied to the CDM structures while the variation in the temperature should be applied to the balloon shaped structure at the same time.

Simulation for the balloon shaped structure is needed to be performed. The CDM structures with the balloon shaped structure need to be simulated as salinity sensors, temperature sensors and simultaneous sensors, as well.

Study on the cross-sensitivity effect is needed to be studied for the balloon shaped structure, the CDM structures and the combination of both.

4.2 – Published and Accepted Papers

1) Tanushree Selokar and Maria Thereza M. Rocco Giraldi, “All-fiber sensors for salinity and temperature simultaneous measurement”, Optical and Quantum Electronics vol. 53, pp. 01-17, 2021.

2) Tanushree Selokar and Maria Thereza M. Rocco Giraldi, “Study of Core Diameter Mismatch Based optical sensor for Salinity and Temperature”, Latin American Workshop on Optical Fiber Sensor – LAWOFS 2019, July 2019, Brazil.

3) Tanushree Selokar and Maria Thereza M. Rocco Giraldi, “All-fiber Salinity Sensors using CDM Structures”, XLIV OSI Symposium – Frontiers in Optics and Photonics (FOP21), September 2021, India. Online Conference. Accepted Papers.pdf - Google Drive

References

1] J. HECHT, "**City of light: the story of fiber optics**", Oxford University Press, New York, 1999.

2] G. P. AGRAWAL, **Optical Communication: Its History and Recent Progress**", Chapter 8.

3] K. C. KAO, G. A. HOCKHAM, Dielectric-fiber surface waveguides for optical frequencies. **Proc. IEEE**, 113(7):1151–1158, 1966.1

4] http://www.nobelprize.org/nobel_prizes/physics/laureates/2009/

5] F. T. S.YU, P. B. RUFFIN, S. YIN, "**Fiber optic sensor**", vol. 2, CRC Press, Boca Raton, 2008.

6] K. FIDANBOYLU, H. S. EFENDIOGLU, "**Fiber Optic Sensors and Their Applications**", in Proceedings IATS'09, 2009.

7] B. GHOLAMZADEH, H NABOVATI, "Fiber optic Sensor", **International Journal of Electronics and Communication Engineering**, vol. 2, pp. 1107-1117, 2008.

8] Y. DAKIN, AND B. CULSHAW, "**Optical fiber sensors-Principles and components**", vol. I, Artech House, Boston.

9] C. M. DAVIS, E. F. CAROME, M. H. WEIK, S. EZEKIEL, R. E. EINZIG, **Fiber optic sensor technology handbook**, Optical Technologies INC, 1986.

10] E. PINET, Medical applications: Saving lives. **Nature Photonics**, 2(3):150–152, 2008. 5

11] Y. ZHAO, Q. WU, Y. ZHANG, "Simultaneous measurement of salinity, temperature and pressure in seawater using optical fiber SPR sensor", **Measurement,** Vol 148, 1-7, 2019.

12] A. BALAJI GANESH, T. K. RADHAKRISHNAN, "Fiber-Optic pH Sensor", **Fiber and Integrated Optics,** Vol 25, 403–409, 2006

13] J. ZAJÍC, L. TRAPLOVÁ, V. MATĚJEC, M. POSPÍŠILOVÁ, I. BARTOŇ, "Optical pH Detection with U-Shaped Fiber-Optic Probes and Absorption Transducers", **Conference Papers in Science,** Vol 2015, Article ID 513621, 8.

14] R. CHEN, C. E. W. HAHN, A. D. FARMERY, "A flowing liquid test system for assessing the linearity and time response of rapid fibre optic oxygen partial pressure sensors", **Respiratory Physiology & Neurobiology,** Vol 183, 100-107, 2012.

15] G. Y. CHEN, N. X. L. ZHANG, G. BRAMBILLA, T. P. NEWSON, "Enhanced responsivity of a flexural disc acceleration sensor based on optical microfiber**", Optics Communications,** Vol 285, 4709-4714, 2012.

16] B. SHANGA, Y. MIAOA, H. ZHANGA, B. LIA, K. ZHANGA, C, FEIB,"High-sensitivity dual-direction weak magnetic field sensor based on structural modulated ultralong period microfiber grating", **Optics and Laser Technology,** Vol 134, 106572, 2021.

17] R. X. GAO, Q. WANG, F. ZHAO, B. MENG, S. L. QU, “Optimal design and fabrication of SMS fiber temperature sensor for liquid”, **Optics Communications,** Vol 283, 3149–3152, 2010.

18] L. SCHENATO, A. GALTAROSSA, A. PASUTO, L. PALMIERI, “Distributed optical fiber pressure sensors”, **Optical Fiber Technology,** Vol 58, 102239, 2020.

19] Z. YIXIN, C. YINSEN, X. FEI, Z. MISHENG, S. YUANYUAN, W. SHUN, X. WEIHONG, Z. MOHAMMADMASOUD, W. JIANLING, Z XUPING, “A hybrid distributed optical fibre sensor for acoustic and temperature fields reconstruction”, **Optics Communications**, Vol 435,134–139, 2019.

20] S. ZHANGA, J. HEB, Q. YUB, X WU, “Multi-scale load identification system based on distributed optical fiber and local FBG-based vibration sensors”, **Optik - International Journal for Light and Electron Optics,** Vol 219, 165159, 2020.

21] S. P. CHEWA, A. Z. ZULKIFLI, H. HAMADD, S. W. HARUNA, L. Y. LEEE, H. A. RAZAK, F. R. M. ADIKANA, “Singlemode-multimode-singlemode fiber structure as compressive strain sensor on a reinforced concrete beam”, **Optik,** Vol 154, 705–710, 2018.

22] H. Y. ZEBIAN, H. J. TAHER, “Relative humidity sensor based on no-core multimode interferometer coated with Al2O3-PVA composite films”, **Optical Fiber Technology**, Vol 54, 102110, 2020.

23] H. WANG , L. JIANG, P. XIANG, “Priority design parameters of industrialized optical fiber sensors in civil engineering”, **Optics and Laser Technology**, Vol 100, 119–128, 2018.

24] A. SURKOVA, V. PANCHUK, V. SEMENOV, V. PROTOSHCHAK, E. KARPUSHCHENKO, A. SLEPTSOV, A. LEGIN, D. KIRSANOV, “Low-cost optical sensor for real-time blood loss monitoring during transurethral surgery”, **Optik**, Vol 228, 166148, 2021.

25] H. KHLAIFI, A. ZRELLI, T. EZZEDINE, “Optical fiber sensors in border detection application: Temperature, strain and pressure distinguished detection using fiber Bragg grating and fluorescence intensity ratio”, **Optik,** Vol 229, 166257, 2021.

26] P. RAYA, B. SRINIVASANA, K. BALASUBRAMANIAMB, P. RAJAGOPAL, “Monitoring pipe wall integrity using fiber Bragg grating-based sensing of low-frequency guided ultrasonic waves”, **Ultrasonics**, Vol 90, 120–124, 2018.

27] L. ZOU, X. BAO, F. RAVET, L. CHEN, “Distributed Brillouin fiber sensor for detecting pipeline buckling in an energy pipe under internal pressure” **Applied Optics**, Vol 45(14), 3372–3377, 2006.

28] L. ZOU, G. A. FERRIER, S. AFSHAR V., Q. YU, L. CHEN, X. BAO, “Distributed Brillouin scattering sensor for discrimination of wall-thinning defects in steel pipe under internal pressure” **Applied Optics**, Vol 43(7), 1583–1588, 2004.

29] S. C. HUANG, W. W. LIN, M. T. TSAI, AND M. H. CHEN, “Fiber optic in-line distributed sensor for detection and localization of the pipeline leaks”, **Sensors and Actuators A**, Vol 135, 570–579, 2007.

30] F. TANIMOLA, D. HILL, “Distributed fibre optic sensors for pipeline protection”, **Journal of Natural Gas Science and Engineering**, Vol 1, 134–143, 2009.

31] R. BERNINI, A. MINARDO, L. ZENI, “Vectorial dislocation monitoring of pipelines by use of Brillouin-based fiber-optics sensors”, **Smart Materials and Structures**, Vol 17(1), 015006, 2008.

32] M. JONES, “Structural-health monitoring: A sensitive issue”, **Nature Photonics**, Vol 2(3), 153– 154, 2008.

33] L. DONGSHENG, S.-C. M. HO, S. GANGBING, R. LIANG, L. HONGNAN, “A review of damage detection methods for wind turbine blades”, **Smart material and structures,** Vol 24(3), 2015.

34] J. A. C. HEIJMANS, L. K. CHENG, F. P. WIERINGA, “Optical fiber sensors for medical applications – Practical engineering considerations”, **Springer, IFMBE Proceedings**, Vol 22, 2330–2334, 2008.

35] M. E. BOSCH, A. J. R. SANCHEZ, F. S. ROJAS, C. B. OJEDA, “Recent development in optical fiber biosensors”, **Sensors**, 7:797–859, 2007. 6

36] R. WOLTHUIS, D. MCCRAE, E. SAASKI, J. HARTL, G. MITCHELL, “Development of a medical fiber-optic pH sensor based on optical absorption”, **IEEE Transactions on Biomedical Engineering**, Vol 39(5):531–537, 1992.6

37] R. A. WOLTHUIS, D. MCCRAE, J. C. HARTL, E. SAASKI, G. L. MITCHELL, K. GARCIN, R. WILLARD, “Development of a medical fiber-optic oxygen sensor based on optical absorption change”, **IEEE Transactions on Biomedical Engineering**, Vol 39(2),185–193, 1992.

38] P. A. E. PIUNNO, U. J. KRULL, R. H. E. HUDSON, M. J. DAMHA, H. COHEN, “Fiber optic biosensor for fluorimetric detection of DNA hybridization”, **Analytica Chimica Acta**, Vol 288(3), 205–214, 1994.

39] P. A. E. PIUNNO, U. J. KRULL, R. H. E. HUDSON, M. J. DAMHA, H. COHEN, “Fiber Optic DNA sensor for fluorometric nucleic acid determination”, **Analytical Chemistry**, Vol 67. 6.

40] Y. ZHANG, X. CHEN, Y. WANG, K. L. COOPER, A. WANG, “Microgap multicavity Fabry-Perot biosensor”, Journal of Lightwave Technology, Vol 25(7), 1797–1804, 2007.

41] Q. MENG, X. DONG, K. NI, Y. LI, B. XU, AND Z CHEN, “Optical Fiber Laser Salinity Sensor Based on Multimode Interference Effect”, **IEEE Sensors Journal**, Vol 14, 1813-1816, 2014.

42] J. WANG, B. CHEN, “Experimental research of optical fiber sensor for salinity measurement”, **Sensors and Actuators A: Physical**, Vol. 184, 53-56, 2012.

43] Y. QIAN, Y. ZHAO, Q. WU, Y. YANG, “Review of salinity measurement technology based on optical fiber sensor”, **Sensors and Actuators B: Chemical**, Vol 260, 86-105, 2018.

44] M. F. JADDOA, A. A. JASIM, M. Z. A. RAZAK, S. W. HARUN, H. AHMAD, “Highly responsive NaCl detector based on inline microfiber Mach–Zehnder interferometer”, **Sensors and Actuators A: Physical**, Vol. 237, 56-61, 2016.

45] Z. HONGLING, C. BITONG, Z. FANG, Q YUEFENG, H. TINGNAN, “Simultaneous measurement of refractive index and temperature by Mach–Zehnder cascaded with FBG sensor based on multi-core microfiber”, **Optics Communications**, Vol 493, 126985, 2021.

46] Z. XIAOLI, D. MINGLI, Z. YUMIN, L. FEI, Z LIANQING, “Simultaneous measurement of strain, temperature and refractive index based on a fiber Bragg grating and an in-line Mach–Zehnder interferometer”, **Optics Communications,** Vol 435, 61–67, 2019.

47] L. TIEGEN, C. YAOFEI, H. QUN, L. FANGCHAO, Y. YUNZHI, “Sensor based on macro bent fiber Bragg grating structure for simultaneous measurement of refractive index and temperature” Vol. 55, No. 4, 2016, **Applied Optics**, 791-795.

48] Y. XIUJUAN, C. XUEFENG, B. DAN, Z. JINTAO, L. SHENGCHUN, “In-Fiber Modal Interferometer for Simultaneous Measurement of Refractive Index and Temperature” **IEEE Photonics Technology Letters**, vol. 28, no. 2, 2016, 189-192.

49] A. D. D. LE, J. HWANG, M. YUSUF, K. H. PARK, S. PARK, J. KIM, “Simultaneous Measurement of Humidity and Temperature with Cytop reduced Graphene Oxide-overlaid Two-mode Optical Fiber Sensor”, **Sensors and Actuators B**, 126841,1-36, 2019.

50] B. YUNLONG, Y. BIN, L. CHAO, L. SHUO, L. YUDONG, J. SHUISHENG, “Simultaneous Measurement of Refractive Index and Temperature Based on NFN Structure”, **IEEE Photonics Technology Letters**, Vol. 26(21), 2193-2196, 2014.

51] Y. LIAO, J. WANG, S. WANG, H. YANG, X. WANG, “Simultaneous measurement of seawater temperature and salinity based on microfiber MZ interferometer with a knot resonator”, **J. Lightwave Technol**, Vol 34(23), 5378–5384, 2016.

52] M BLAHUT, D KASPRZAK, “Multimode interference structures – properties and applications”, **Optica Applicata**, vol 34, pp 573-587, 2004.

53] L. B. SOLDANO, E. C. M. PENNINGS, “Optical multi-mode interference devices based on selfimaging: principles and applications”, **Journal of Lightwave Technology**, Vol.13, 615–627, 1995.

54] Q WU, Y SEMENOVA, A. M. HATTA, P WANG, G FARRELL, “Singlemode-multimode-singlemode fiber structures for simultaneous measurement of strain and temperature”, **Microwave and Optical Technology Letters**, Vol 53, 2181-2185, 2011.

55] S. SILVA, E G. P. PACHON; M. A. R. FRANCO, P. JORGE, J. L. SANTOS, F. X. MALCATA, C M. B. CORDEIRO, O. FRAZÃO, “Curvature and Temperature Discrimination Using Multimode Interference Fiber Optic Structures – A Proof of Concept”, **Journal of Lightwave Technology**, Vol. 30, pp. 3569–3575, 2012.

56] Q. WANG, G. FARRELL, W. YAN, “Investigation on Single-Mode–Multimode–Single-Mode Fiber Structure”, **Journal of Lightwave Technology**, Vol. 26, 512-519, 2008.

57] E. G. P. PACHON, **Dispositivos em fibras ópticas baseados em interferência multimodal**. Dissertação de mestrado. Campinas, SP: Unicamp, 2013.

58] A. M. HATTA, **Singlemode-Multimode-Singlemode optical fibre structures for optical sensing**. PhD Thesis. Dublin – Ireland: School of Electronic and Communications Engineering – Faculty of Engineering – Dublin Institute of Technology, 2009.

59] MOHAMMED, W. S.; MEHTA, A.; JOHNSON, E. G, “Wavelength tunable fiber lens based on multimode interference”, **Journal of Lightwave Technology**, Vol 22(2), 469-477, 2004.

60] H. Y. CHOI, M. J. KIM, B. H. LEE, “All-fiber Mach–Zehnder type interferometers formed in photonic crystal fiber”, **Opt. Exp.,** Vol. 15, 5711–5720, 2007.

61] L. COELHO, J. KOBELKE, K. SCHUSTER, O. FRAZÃO, “Multimode interference in outer cladding large-core air-clad photonic crystal fiber”, **Microwave and Optical Technology Letters**, Vol 54, 1009-1011, 2012.

62] J. VILLATORO, D. MONZÓN-HERNÁNDEZ, “Low-Cost Optical Fiber Refractive-Index Sensor Based on Core Diameter Mismatch”, **Journal of Lightwave Technology**, Vol. 24, 1409-1412, 2006.

63] BRYNGDAHL, “Image formation using self-imaging techniques”, **Journal Optical Science. Amer**, Vol. 63, 41-19, 1973.

64] C. S. FERNANDES, M. T. M. R. GIRALDI, C. J. GOUVEIA, M. J. DE SOUSA, J. C. W. A. COSTA, “Remote curvature fiber sensors using core mismatch structures and OTDR based interrogation”, **In: Proc. of the II International Conference on Applications of Optics and Photonics. Aveiro: SPIE Digital Library**, Vol. 1,173-176, 2014.

65] A. H. E. MORSHED, M. Y. SHALABY, “Bending Characteristics of Single Mode-

Multimode-Single Mode Optical Fiber Structures", **31st National Radio Science Conference** (NRSC2014), Egypt, 2014.

66] D. MARCUSE, "**Light Transmission Optics**", Van Nostrand Reinhold, New York, 1972.

67] R. ULRICH, "Image formation by phase coincidences in optical waveguides", **Optics Communications**, Vol. 13, 259-264, 1975.

68] R. ULRICH, "Light-propagation and imaging in planar optical waveguides", Nouv. Rev. Optique, Vol. 6, 253-262, 1975.

69] A. H. MORSHED, "Self-imaging in Single mode-Multimode-Single mode Optical Fiber Sensors", **IEEE**, Vol. 10,1-5, 2011

70] K. OKAMOTO, "**Fundamentals of Optical Waveguides**", 2nd edition, 2006.

71] Z. TONG, J. SU, Y. CAO, W. ZHANG, "Simultaneous measurement based on composite interference structure", **IEEE Photonics Technology Letters**, Vol 26, 1310–1313, 2014.

72] L. Xu, Z. Yong, L. Ri-Qing, W. Qi, "High Sensitivity Balloon-Like Interferometer for Refractive Index and Temperature Measurement", **IEEE Photonics Technology Letters**, Vol. 28, 1485-1488, 2016.

73] L. ZHAO, B. LIU, Y. WU, T. SUN, Y. MAO, T. NAN, "Measurement of refractive index and temperature using balloon shaped Mach-Zehnder interferometer", **Optik - International Journal for Light and Electron Optics**, Vol. 188, 115–119, 2019.

74] SYNOPSYS INC. BeamPROP v2013.12 - User Guide, 2013.

75] L. NGUYEN, M. VASILIEV, K. ALAME, "Three-wave fiber Fabry-Perot interferometer for simultaneous measurement of temperature and water salinity of seawater", **Opt. Express**, Vol 23(7), 450–452, 2011.

76] C. WU, L. SUN, J. LI, B. O. GUAN, "Highly sensitive evanescent-wave water salinity sensor realized with rectangular optical microfiber Sagnac interferometer", **International Conference on Optical Fiber Sensor**, 9157, 2014.

77] Y. ZHAO, Q. WU, Y. ZHANG, "Theoretical analysis of high-sensitive seawater temperature and salinity measurement based on C-type micro-structured fiber", **Sensors Actuators. B Chemical**, Vol 258(1), 822–828, 2018.

78] T. LIU, Y. CHEN, Q. HAN, F. LIU, Y. YA, "Sensor based on macrobent fiber Bragg grating structure for simultaneous measurement of refractive index and temperature", **Applied Optics**, Vol 55(4), 791–795, 2016.

79] X. ZHANG, W. PENG, "Bent-fiber intermodal interference based dual channel fiber optic refractometer", **Optics Express**, Vol 23(6),7602–7610, 2015.

80] K. TIAN, G. FARRELL, W. YANG, X. WANG, E. LEWIS, P. WANG, "Simultaneous measurement of displacement and temperature based on a balloon-shaped bent SMF structure

incorporating an LPG", **Journal Lightwave Technology**, Vol 36(20), 4960–4965, 2018.

81] L. ZHAO, B. LIU, Y. WU, T. SUN, Y. MAO, T. NAN, "Measurement of refractive index and temperature using balloon shaped Mach–Zehnder interferometer", **Optik Int. Journal. Light. Electron. Opt**, Vol 188, 115–119, 2019c.

Appendix

Beam Propagation Software

In Symbol Table editor, the variables are defined as shown in figure 56. In the launch parameter, the optical filed injected in the fiber can be selected such as gaussian mode, launch power and many other options are available where a separate file or an edited file can also be used as illustrated in figure 57.

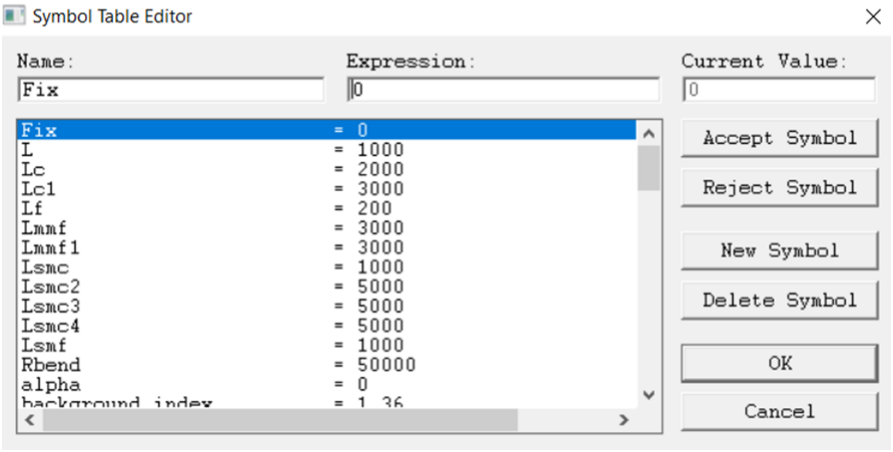


Figure 56 – Edit symbol Parameter window.

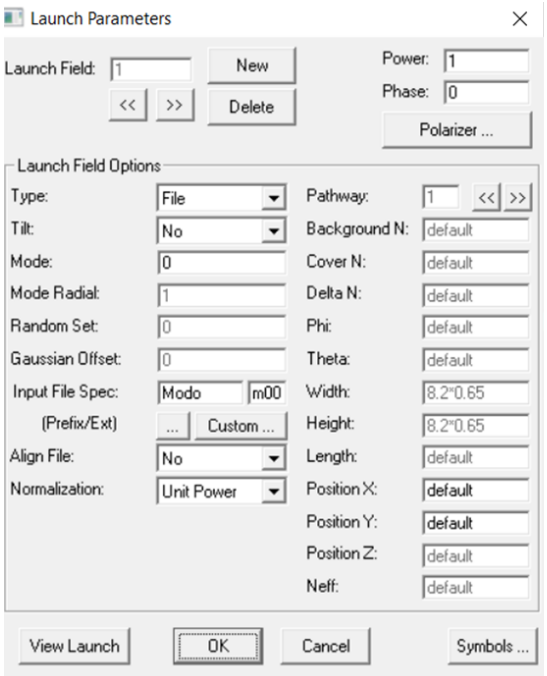


Figure 57 – Setting of launch parameter with different launch field.

The pathway monitor tool as shown in figure 58 is useful to analyze the field in standard physical quantities such as the optical power in a particular region of the circuit or the power traveling in a particular mode. Figure 59 shows in green the chosen pathway for the SMS sensor model.

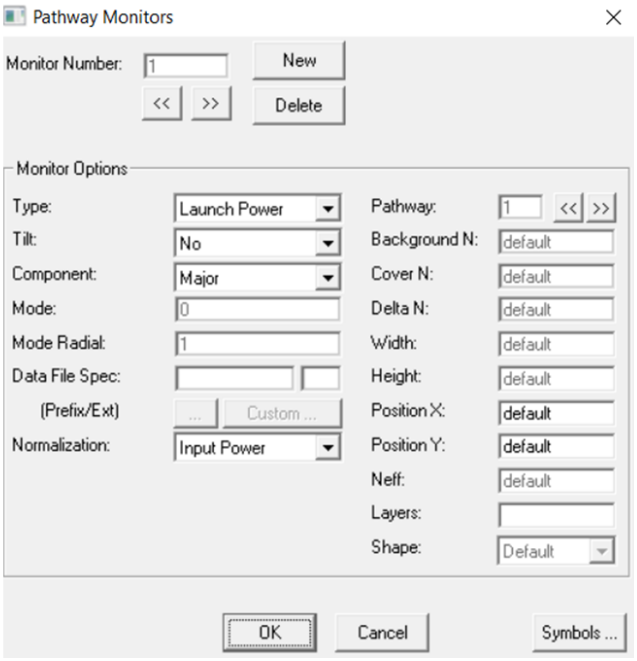


Figure 58 – Pathway monitor window.

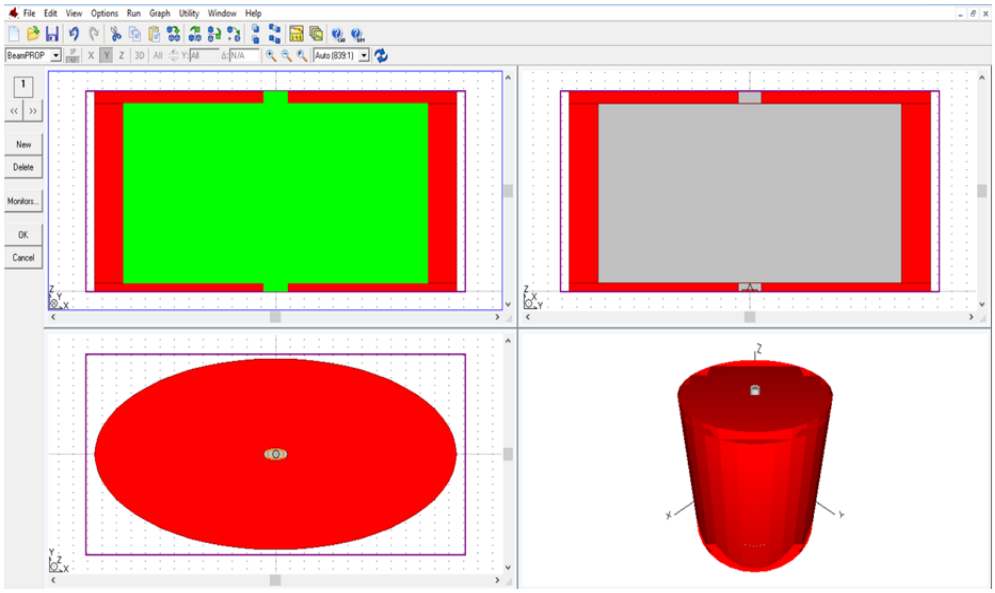


Figure 59 – Pathway shown in the model of the SMS.

In the launch MOST optimizer the parameters can be changed in steps, in the given case background index is changed. The MOST parameter window is shown in figure 60.

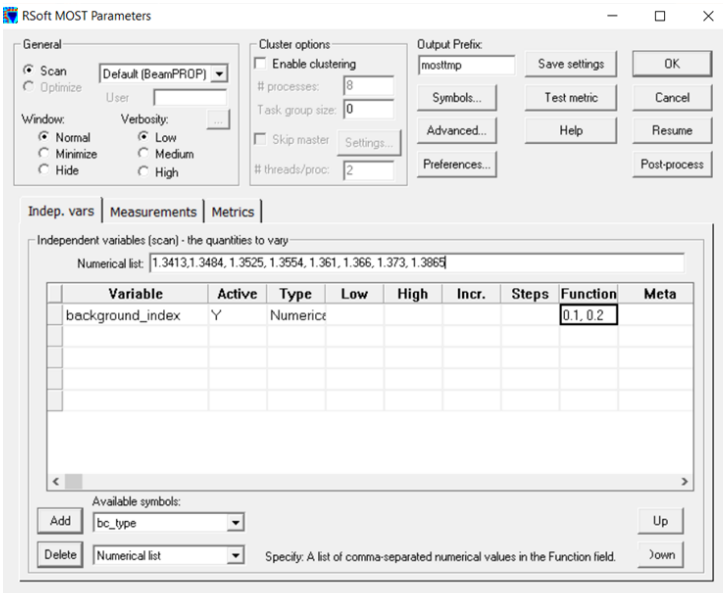


Figure 60 – Launch MOST optimizer / scanner window.